Electronic Supplementary Information

Superior performance enabled by supramolecular interactions in metal−organic cathode: the power of weak bonds

An-Che Li,‡ [a] Cheng-Han Chang,‡[b] Alexander S. Ivanov,[c] Yi-An Lo,[a] Ilja Popovs,[c] Jeng-Lung Chen,[d] Yu-Chun Chuang,[d] Yu-Chung Chang,[d] Bo-Hao Chen,[d] Jui-Chin Lee,[e] Teng-Hao Chen*[f] and Watchareeya Kaveevivitchai*[a]

a. Department of Chemical Engineering, National Cheng Kung University, Tainan City 70101, Taiwan; Hierarchical Green-Energy Materials Research Centre, National Cheng Kung University, Tainan City 70101, Taiwan
b. Department of Chemistry, Tamkang University, New Taipei City 25137, Taiwan
c. Chemical Sciences Division, Oak Ridge National Laboratory, Oak Ridge, P.O. Box 2008, TN 37831, USA
d. National Synchrotron Radiation Research Centre, Hsinchu 30076, Taiwan
e. Core Facility Centre, National Cheng Kung University, Tainan City 70101, Taiwan
f. School of Pharmacy, National Cheng Kung University, Tainan City 70101, Taiwan
‡. These authors contributed equally to this work.

*To whom correspondence should be addressed. E-mail: thchen@gs.ncku.edu.tw, wkaveechai@mail.ncku.edu.tw

General Methods and Materials

Starting materials and solvents were purchased and used without further purification from commercial suppliers (Sigma-Aldrich and TCI). Fourier-transform infrared (FT-IR) spectra were recorded on Nicolet iS5 or Nicolet 6700, Thermo Scientific. In-house powder X-ray diffraction (PXRD) patterns were collected on Bruker D8 Advance ECO. Single-crystal X-ray diffraction experiments were performed by using Bruker D8 Venture dual X-ray single crystal diffractometer. Thermogravimetric analysis (TGA) was carried out on a TA Instrument TGA 2050 from 25 to 900 °C with a ramping rate 20 °C min^{-1} under the flow of N_2. X-ray photoelectron spectroscopy (XPS) measurements were done using ULVAC PHI 5000 VersaProbe III equipped with an Al Kα (1487 eV) as a radiation source. Survey scans were collected with a pass energy of 100 eV, followed by high-resolution scans with a pass energy of 20 eV. All spectra were charge-corrected relative to the C 1s component at 284.7 eV binding energy, and analyzed using CasaXPS software. High-resolution transmission electron microscopy (HR-TEM) was carried out on JEOL JEM-2010 electron microscope. Elemental analysis was performed on Elementar Vario EL III.

Synthesis of $[\text{CuL(Py)}_2]_n$ Coordination Polymer (CP)

1,4-dicyano-2,3,5,6-tetrahydroxybenzene (LH_4, 180 mg, 0.9 mmol) and $Cu(NO_3)_2{\cdot}3H_2O$ (215 mg, 0.9 mmol) were dissolved in 100 mL of *N*,*N*-dimethylformamide (DMF) and sonicated for 5 min. Then 20 mL of pyridine was added. The solution was transferred into a 100 mL bottle and heated in a 100 °C oven for 48 h. After cooling down, orange single crystals were obtained. The crystals were washed with DMF (3 × 5 mL) and ethyl acetate (3 × 5 mL), and dried in vacuum at 80 °C for 3 h. Yield calculated from the dried sample was 68 % based on Cu. FT-IR: 2218 (s, $\tilde{\nu}_{C\equiv N}$), 1636 (s, $\tilde{\nu}_{C=O}$) cm^{-1}. Anal. calcd (%) for $CuC_{18}H_{10}N_4O_4$: C 52.75, H 2.46, N 13.67; Found: C 52.47, H 2.42, N 13.77. CCDC 2089952 contains the supplementary crystallographic data for this paper. These data are provided free of charge by the Cambridge Crystallographic Data Centre.

Electrochemical Measurements

$[\text{CuL(Py)}_2]_n$ crystals were mixed and ground with conductive carbon (Ketjen black) and PVDF in a 3:6:1 weight ratio, respectively. The mass loading of the active material was kept at ~0.7 mg corresponding to ~1 mg cm^{-2} (for 3:6:1 ratio). Other electrode ratios were also used, 4:5:1, 5:4:1, 6:3:1 and 7:2:1, for comparison. *N*-methyl-2-pyrrolidinone (NMP) was added to form a slurry which was coated onto carbon paper (EP40) current collector. The electrodes were dried in vacuum at 100 °C overnight. CR2032 coin cells were assembled by using Li metal anode, 1 M $LiPF_6$ in 1:1 v/v ethylene carbonate (EC)/ dimethyl carbonate (DMC) electrolyte solution, and Celgard separator. The electrochemical testing was carried out with an Arbin battery cycler and a VMP3 system (BioLogic) at various current densities. Galvanostatic intermittent titration technique (GITT) was performed by alternating 20 mA g^{-1} pulses (15 min) with relaxation periods (3 h).

Cu K-edge X-ray Absorption Spectroscopy (XAS) Measurements

In situ and *ex situ* Cu K-edge XAS measurements were performed at beamline TPS 44A at National Synchrotron Radiation Research Centre (NSRRC), Taiwan. The data were collected in transmission mode and the Cu foil was used as reference for the energy calibration. The electrodes contained active material, Ketjen black and PVDF (7:2:1 weight ratio with active mass loading of 3-4 mg cm^{-2}). Carbon paper EP40 was used as current collector. 1 M $LiPF_6$ in 1:1 v/v EC/DMC was used as electrolyte, and Celgard as separator. CR2032 coin cells were assembled by using Li metal as anode. *In situ* coin cells were equipped with Kapton windows on both sides. For *in situ* experiments, the XAS spectra were recorded at all the major voltage positions and every 30 min during discharge-charge process (3.2 V → 1.5 V → 4.0 V). Autolab potentiostat PGSTAT204 was used for the *in situ* galvanostatic measurements.

In situ Synchrotron PXRD

In situ synchrotron PXRD measurements were performed at beamline TPS 09A at NSRRC, Taiwan. The 15 keV X-ray source was delivered from an in-vacuum undulator (IU22) and the diffraction patterns were recorded by a position-sensitive detector, MYTHEN 24K. Due to the small gaps between detector modules, two necessary datasets were collected 2° apart and were well calibrated by a NIST standard reference material, LaB_6 (660c). The final data were merged and gridded to give an equal step dataset. The potentiostat, Autolab PGSTAT204, was integrated into beamline control software through EPICS. Simultaneous measurements of XRD and galvanostatic process were performed. Electrode ratio of 70 wt% active material, 20 wt% Ketjen black and 10 wt% PVDF with active mass loading of 3-4 mg cm^{-2} was used with carbon paper EP40 as current collector. 1 M $LiPF_6$ in 1:1 v/v EC/DMC was used as electrolyte, and Celgard as separator. CR2032 coin cells were assembled by using Li metal as counter electrode. *In situ* CR2032 coin cells were equipped with Kapton windows. The data were collected every 780 s starting from open circuit voltage to 1.5 V, followed by charging to 4.0 V.

Electrode Mechanistic Studies

The CP electrodes for *ex situ* XPS, FT-IR and HR-TEM contained 70 wt% active material, 20 wt% Ketjen black and 10 wt% PVDF with active mass loading of 3-4 mg cm^{-2}. Stainless steel was used as current collector. 1 M $LiPF_6$ in 1:1 v/v EC/DMC was used as electrolyte. CR2032 coin cells were assembled by using Li metal as counter electrode and Celgard as separator. For all the *ex situ* measurements, the electrodes were cycled to various states of charge and the cells were disassembled in an argon-filled glovebox. For XPS and FT-IR, the electrodes were washed with DMC and dried in vacuum overnight at room temperature. For HR-TEM, the electrode material was scraped off the current collector and sonicated in DMC before dropping onto TEM grids. All the samples were handled without any exposure to air.

Density Functional Theory (DFT) Simulation

First-principles periodic calculations based on DFT were employed to obtain insight into the stepwise Li insertion mechanism using the Vienna Ab-initio Simulation Package (VASP).[1-4] The valence electronic states were expanded in a basis of plane waves, while the core-valence interactions were described using the Projector Augmented Wave (PAW) approach[5,6] with the following valence electron configurations: C (2s, 2p), H (1s), O (2s, 2p), N (2s, 2p), Li (1s, 2s, 2p) and Cu (3d, 4s). Generalized gradient approximation (GGA) of Perdew-Burke-Ernzerhof (PBE)[7] has been adopted for exchange-correlation potential. The DFT-D3 approach of Grimme with zero-damping[8] was used to account for the van der Waals' interactions. Cell optimization of $[CuL(Py)_2]_n$ was carried out starting from the respective X-ray diffraction structure with the plane wave kinetic energy cutoff set to 600 eV, while for the lithiated $[CuL(Py)_2]_n$ structures several Li insertion points were probed with the resultant most energetically stable configurations reported in the main text. During the geometry optimizations, all atomic positions and lattice vectors were fully relaxed. The SCF convergence threshold was set to 10^{-5} eV and a Pulay scheme[9] was used for charge density mixing during the SCF solution. The Brillouin zone was sampled using a well converged Gamma centered *k*-point mesh: (3×2×2). The difference in energy between (3×2×2) and (9×6×6) was 0.73 meV per atom, ensuring good convergence for (3×2×2). Full comparison of the DFT optimized lattice parameters and distances of $[CuL(Py)_2]_n$ and experimental data are provided in Table S4 and S5, respectively.

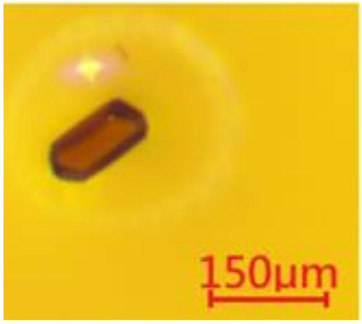

Fig. S1 Photograph of $[CuL(Py)_2]_n$ single crystal.

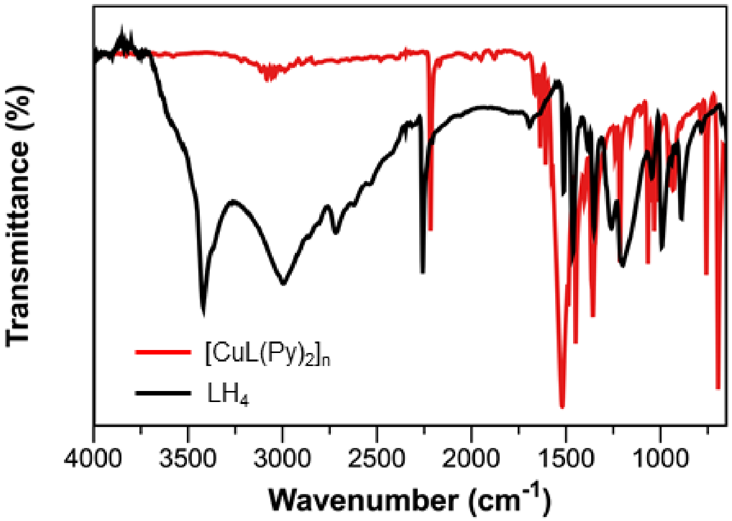

Fig. S2 FT-IR spectra of $[CuL(Py)_2]_n$ and LH_4.

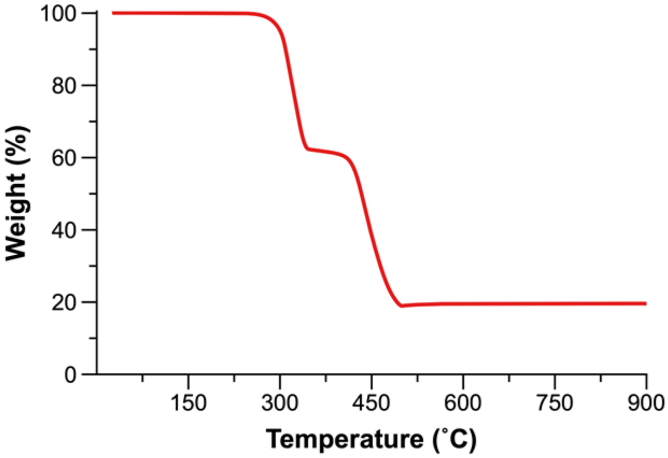

Fig. S3 TGA trace of $[CuL(Py)_2]_n$ revealing high thermal stability, with the loss of the coordinated pyridine molecules at approximately 280 °C, followed by decomposition at 410 °C.

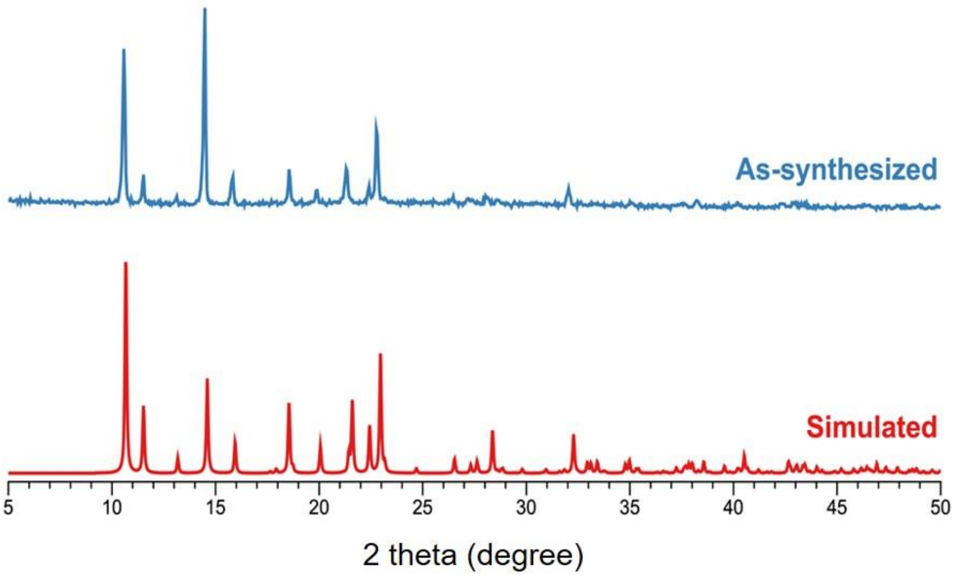

Fig. S4 As-synthesized and simulated PXRD patterns of $[CuL(Py)_2]_n$ exhibiting good agreement which confirms the phase purity of the compound.

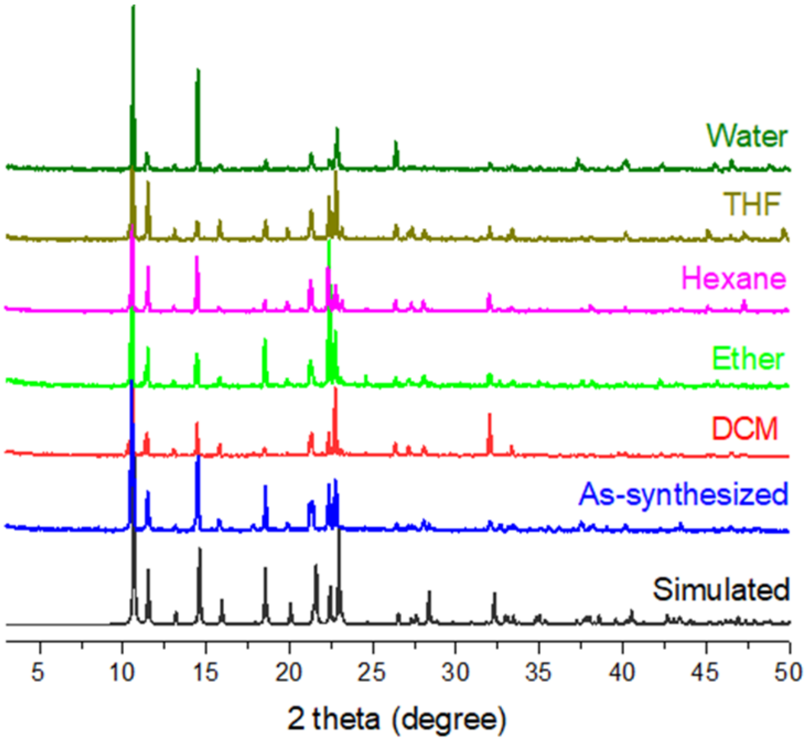

Fig. S5 PXRD patterns of $[CuL(Py)_2]_n$ soaked in different solvents for 24 h revealing that no peak shift is observed, which suggests the structural stability of CP.

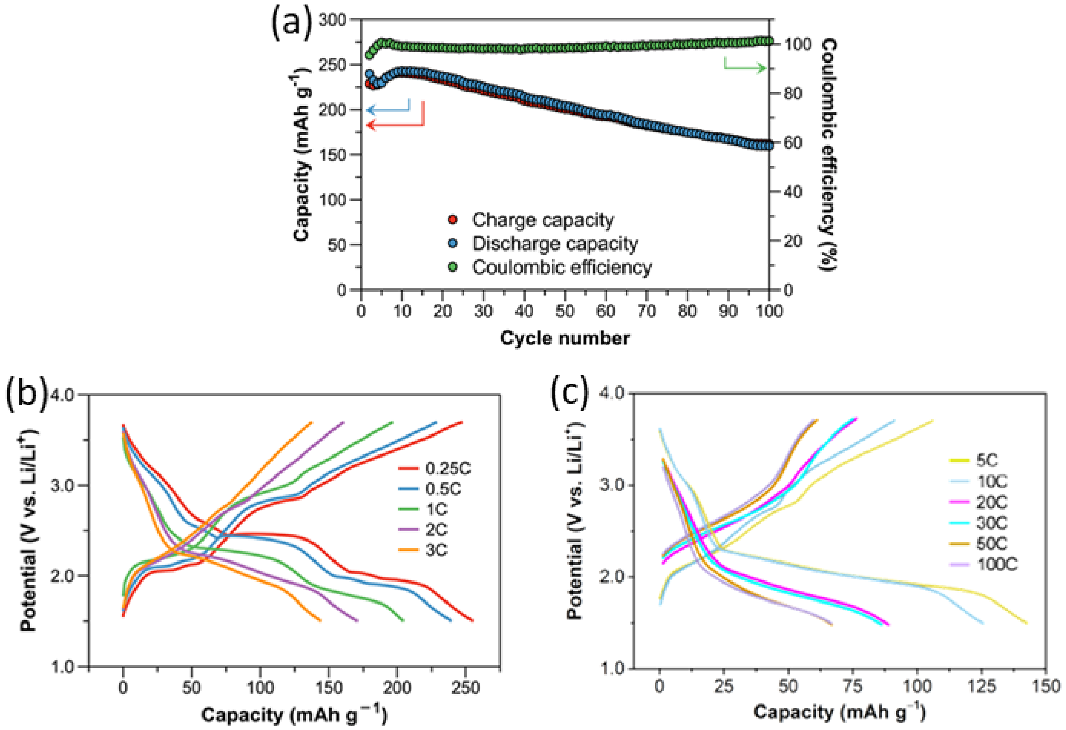

Fig. S6 (a) Capacity retention of [CuL(Py)$_2$]$_n$ electrode in voltage window 1.5−3.7 V at a rate of 0.5C (~131 mA g^{-1}) with Coulombic efficiency. (b) Discharge-charge profiles at rates of 0.25C−3C. (c) Discharge-charge profiles at rates of 5C−100C.

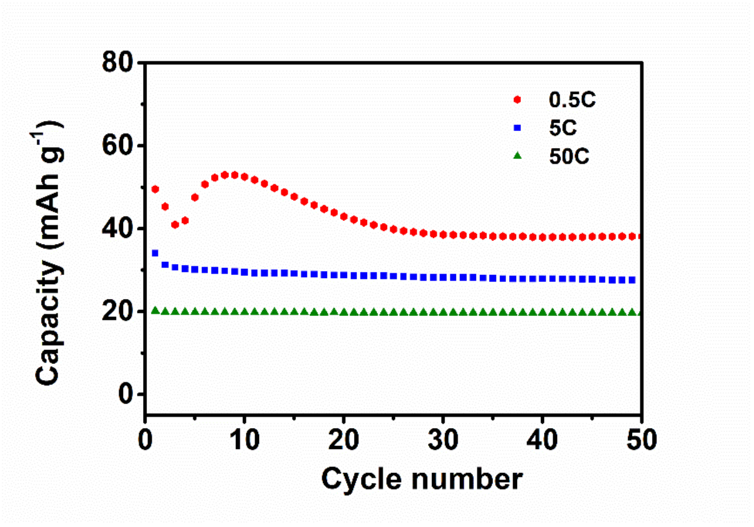

Fig. S7 Electrochemical properties of the conductive carbon (electrode ratio = Ketjen black : PVDF = 9 : 1, with mass loading of Ketjen black ~2 mg cm^{-2}) at 0.5C (~131 mA g^{-1}), 5C (~1308 mA g^{-1}) and 50C (~13081 mA g^{-1}). The delivered capacities of Ketjen black is estimated to be ~40, 30 and 20 mAh g^{-1}, respectively (between 1.5−3.7 V for 90 wt% Ketjen black). These results show a small capacity contribution from the conducting additive especially at high cycling rates.

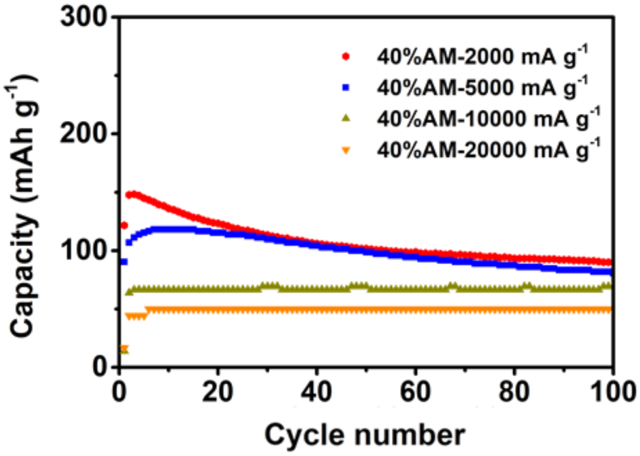

Fig. S8 Discharge capacity retention of $[CuL(Py)_2]_n$ electrodes (40 wt% active material : 50 wt% Ketjen black : 10 wt% PVDF) at current densities ranging from 2000 mA g^{-1} to 20 A g^{-1}.

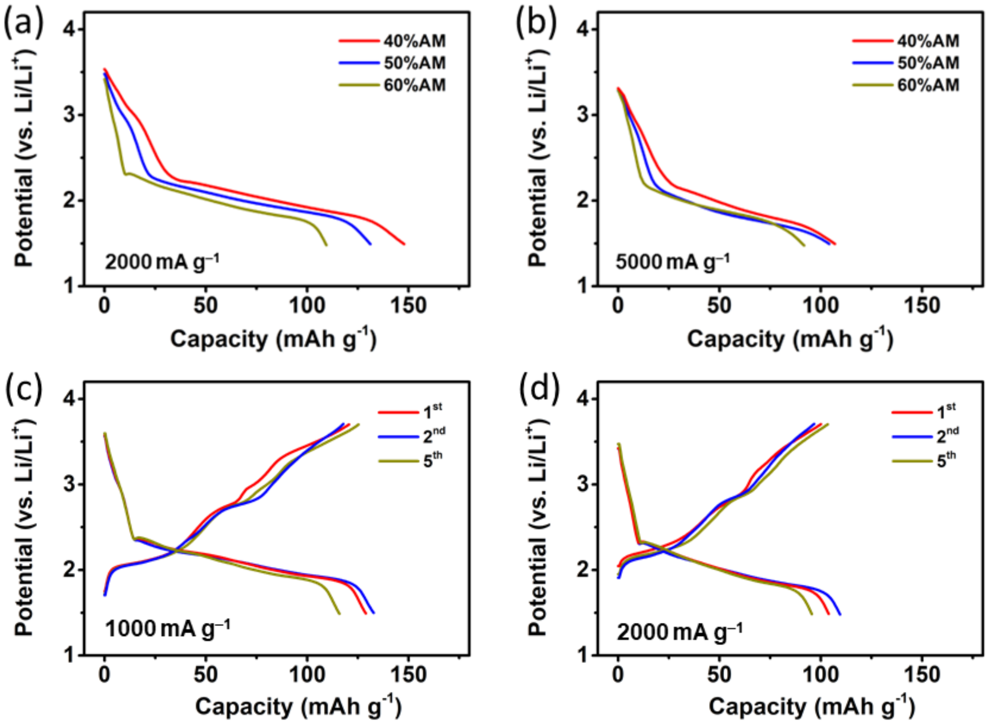

Fig. S9 Discharge profiles of $[CuL(Py)_2]_n$ electrodes with different amounts of active material, 40, 50 and 60 wt%, at (a) 2000 mA g^{-1} and (b) 5000 mA g^{-1} (PVDF was kept constant at 10 wt%). The active mass loading is approximately 2 mg cm^{-2} for 6:3:1 electrode ratio. (c) and (d) Voltage profiles of $[CuL(Py)_2]_n$ electrodes (7:2:1 ratio) for the 1st, 2nd and 5th cycle at 1000 and 2000 mA g^{-1}, respectively.

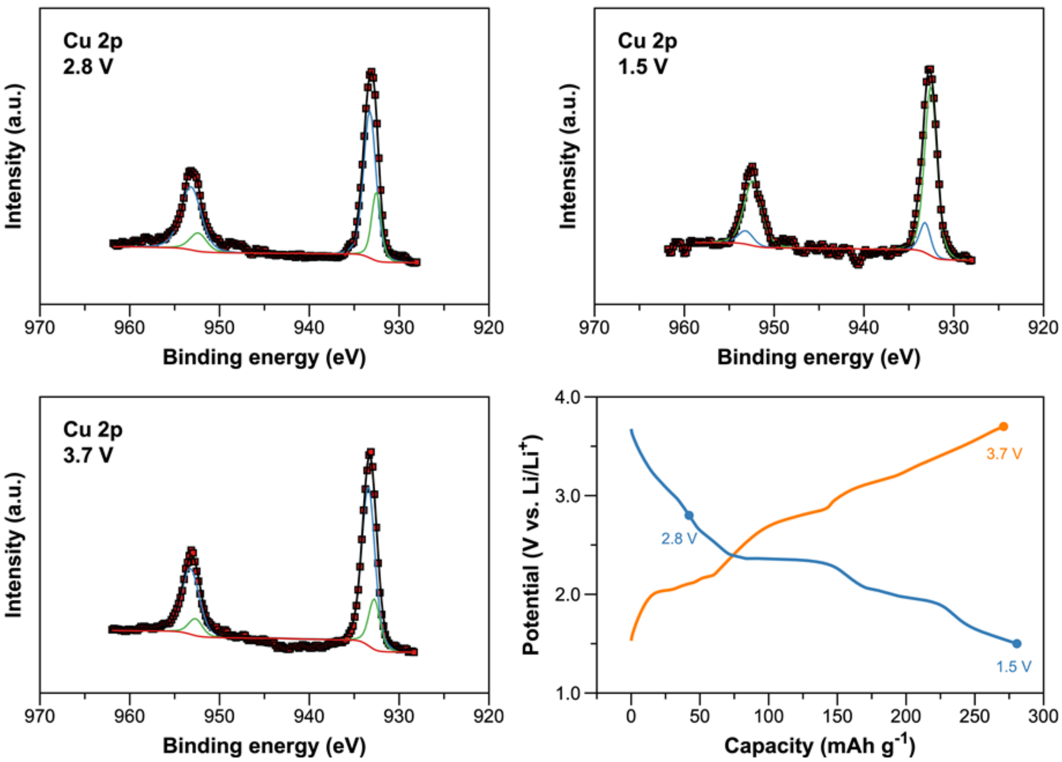

Fig. S10 Deconvolution of the *ex situ* high-resolution Cu $2p_{3/2}$ and $2p_{1/2}$ XPS spectra of CP electrodes at 2.8 and 1.5 V on discharge and 3.7 V on charge at 20 mA g^{-1} (~0.08C) (blue: Cu(I); green: Cu(0)) together with the discharge-charge profile showing the voltage positions.

The deconvolution of the high-resolution Cu 2p spectra of CP electrodes at two voltage positions during the first discharge (2.8 and 1.5 V, Fig. S10) shows the presence of Cu(I) and Cu(0), with Cu $2p_{3/2}$ and Cu $2p_{1/2}$ observed at 933.2 and 953.2 eV for Cu(I) and at 932.6 and 952.5 eV for Cu(0), respectively.[10,11] As the cell is discharged down to the cutoff voltage at 1.5 V at such low rate of 20 mA g^{-1} (~0.08C), more Cu ions are reduced to Cu(0), resulting in the majority being Cu(0). The absence of Cu $2p_{3/2}$ satellite peaks at ~942 eV suggests that there are no Cu(II) species at these two positions. On charge up to 3.7 V, the Cu(0) component becomes significantly smaller with Cu(I) as the main component. This reveals that Cu species are reduced and oxidized during discharge and charge process, respectively. It is worth noting that the degree of redox activity at the Cu metal centre at this low rate has been found to be different from that at high rates as shown in Fig. 3 (main text).

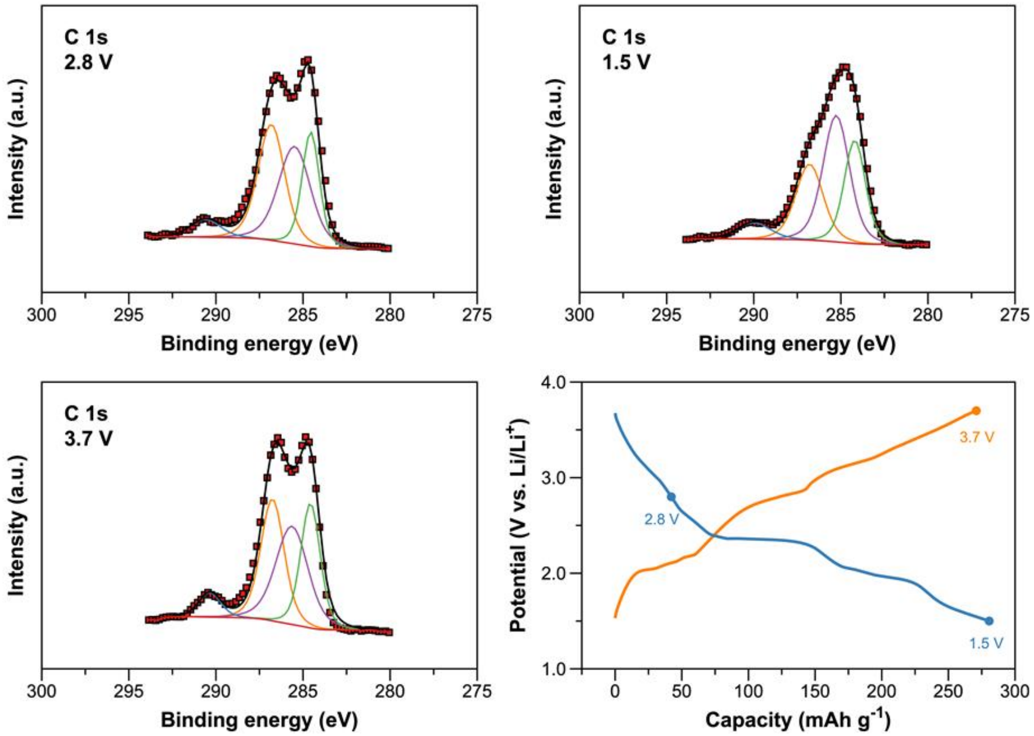

Fig. S11 Deconvolution of the *ex situ* high-resolution C 1s XPS spectra of CP electrodes at 2.8 and 1.5 V on discharge and 3.7 V on charge at 20 mA g^{-1} (~0.08C) (green: C−C; purple: C−O; orange: C=O; blue: assigned to the π−π* satellite peak) together with the discharge-charge profile showing the voltage positions.

The deconvolution of the C 1s XPS spectra (Fig. S11) reveals the redox process of the organic moieties in $[CuL(Py)_2]_n$ at a low rate of 20 mA g^{-1} (~0.08C). The peaks observed at 284.6, 285.5 and 286.8 eV are attributed to C−C, C−O and C=O bonds, respectively.[10,12] On discharge down to 2.8 and 1.5 V, the carbonyl group is transformed into an enol structure as witnessed in the relative ratio between C−O and C=O. C−O component becomes larger as C=O becomes smaller during discharge, while the reverse process occurs on charge up to 3.7 V. This behavior confirms the reversible redox reaction of the organic moieties with the enol structure converting back to carbonyl during charge.

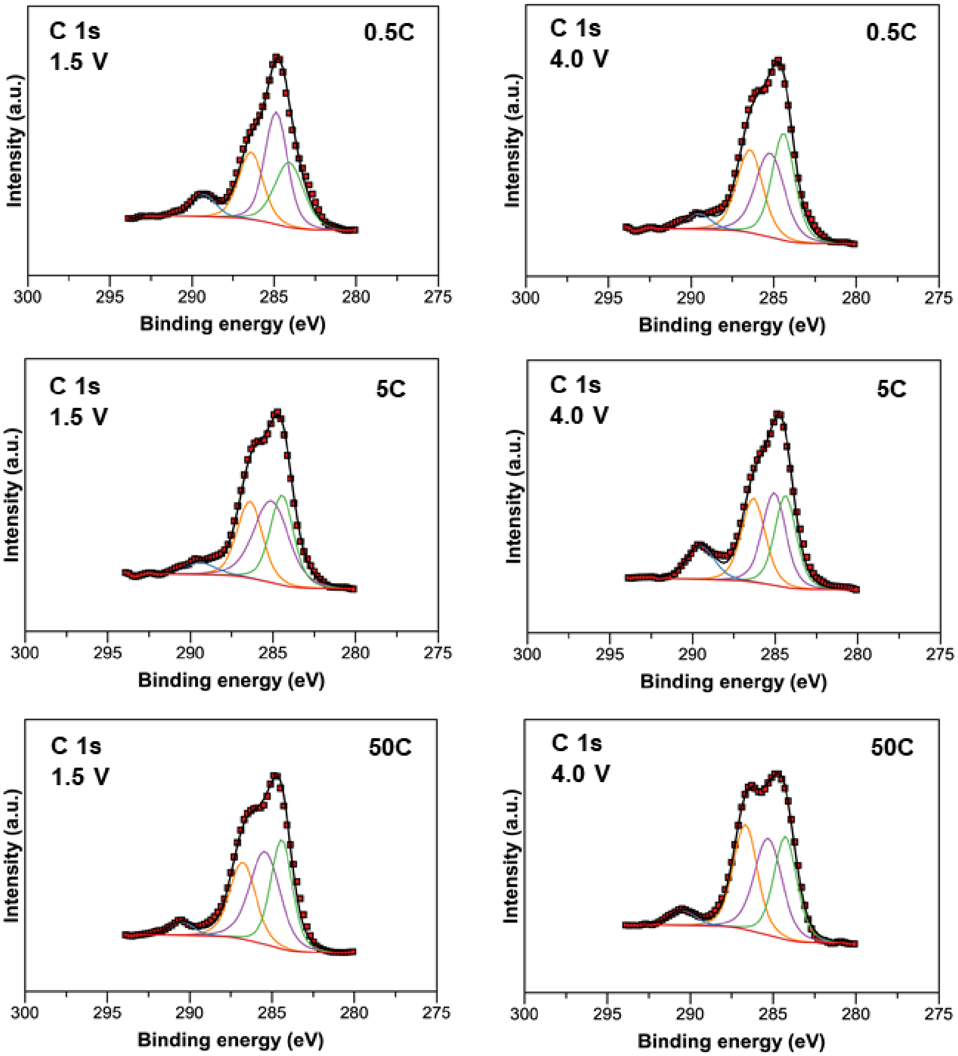

Fig. S12 Deconvolution of the *ex situ* high-resolution C 1s XPS spectra of CP electrodes at 1.5 V on discharge (left) and 4.0 V on charge (right) at 0.5C (top), 5C (middle) and 50C (bottom) (green: C−C; purple: C−O; orange: C=O; blue: assigned to the π−π* satellite peak). These spectra feature the same trend as that mentioned above (Fig. S11) for 0.08C. It is noteworthy that, at 1.5 V, the relative quantity between C−O and C=O decreases from low rate to high rate, which suggests a smaller degree of redox reactions from ligand L, leading to less capacity at a high rate.

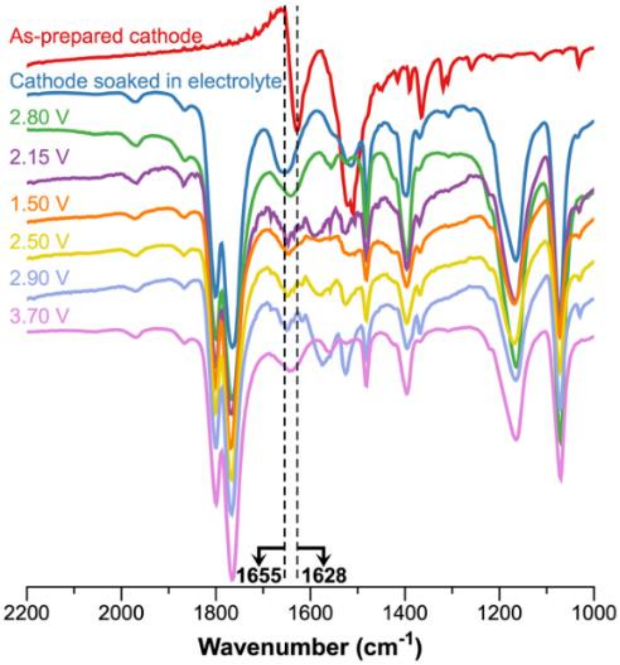

Fig. S13 FT-IR spectra of CP electrodes at different voltage positions (current density: 20 mA g^{-1} or ~0.08C). The coordinating carbonyl groups are observed at 1628 cm^{-1} (as-prepared cathode) and at 1655 cm^{-1} (discharged and charged electrodes). The relative intensity of the carbonyl group decreases on discharge down to 1.5 V, and increases on charge up to 3.7 V. This confirms the change at the redox centers of the organic moieties during cycling, which is in good agreement with the C 1s XPS data.

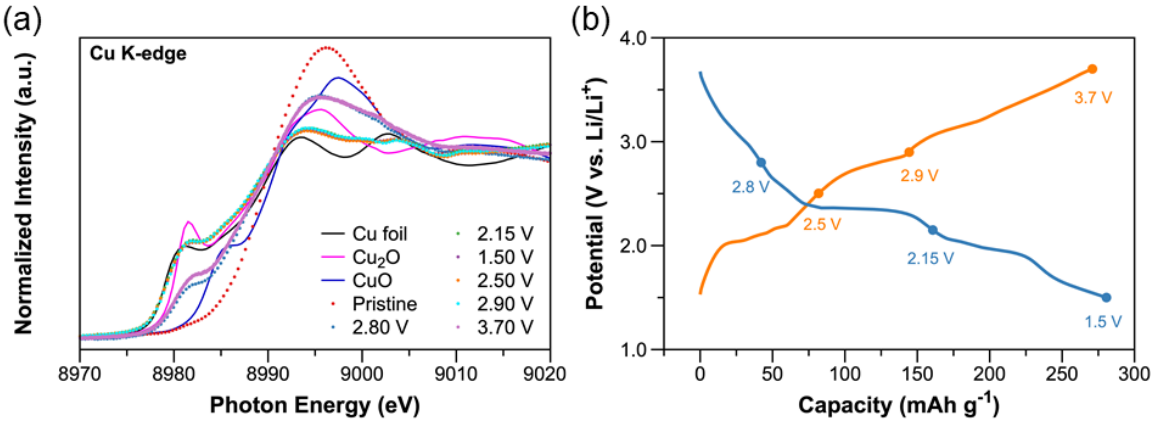

Fig. S14 (a) *Ex situ* Cu K-edge X-ray absorption near edge structure (XANES) of electrodes cycled at 20 mA g^{-1} (~0.08C) together with references. (b) Discharge-charge profile of CP electrode showing the voltage positions. The signal from the pristine electrode confirms the existence of Cu(II) in the material. When the cell is discharged down to 2.80 V, the emergence of a pre-edge peak approximately at 8982 eV and an edge peak shift to a lower energy indicate that Cu(II) ions are reduced.[10,13] Further discharge to 1.5 V and subsequent charge to 3.7 V suggest the redox process of the CP. These results are consistent with the *in situ* XANES data in Fig. 4 (main text).

Extended X-ray Absorption Fine Structure (EXAFS) Analysis

EXAFS analysis of CP electrodes was carried out at Beamline TPS44A in NSRRC, Taiwan. The Cu K-edge EXAFS spectra were collected in transmission mode, using nitrogen-filled gridded ionization chambers[14] with a quick-scanning monochromator at room temperature.[15] The parameters of the local structure around the copper atom were determined by curve-fitting procedures using Artemis[16] data analysis software. For the best-fit parameters of the series of CP electrodes and Cu foil, N is coordination number, R is distance between absorber and backscatter atoms, σ^2 is Debye–Waller factor to account thermal and structure disorders, with R-factor characterizing the goodness of fit. S_0^2 is the amplitude reduction factor which was fixed to 0.778 as determined from Cu foil fitting. Error bounds (accuracies) characterizing the structural parameters obtained by EXAFS data analysis are estimated to be as follows: N, ±20%; R, ±1%; and σ^2, ±20%.

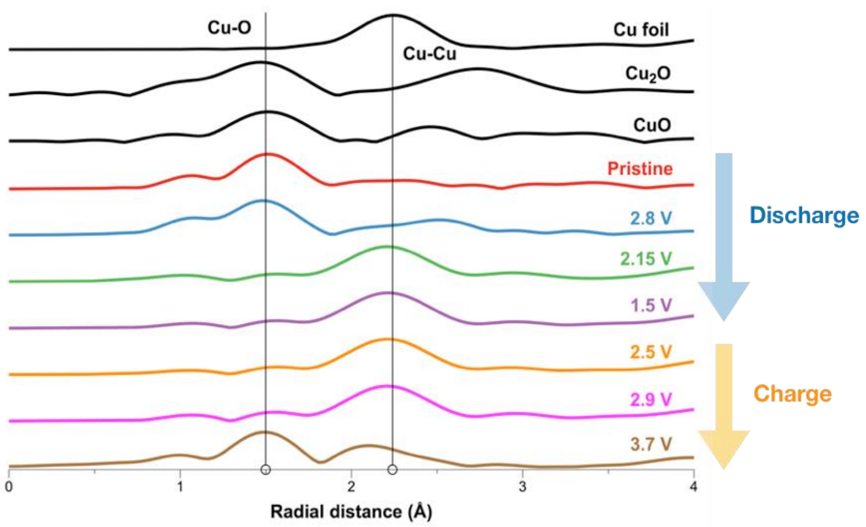

Fig. S15 *Ex situ* Cu K-edge EXAFS of CP electrodes cycled at 20 mA g^{-1} (~0.08C) together with references.

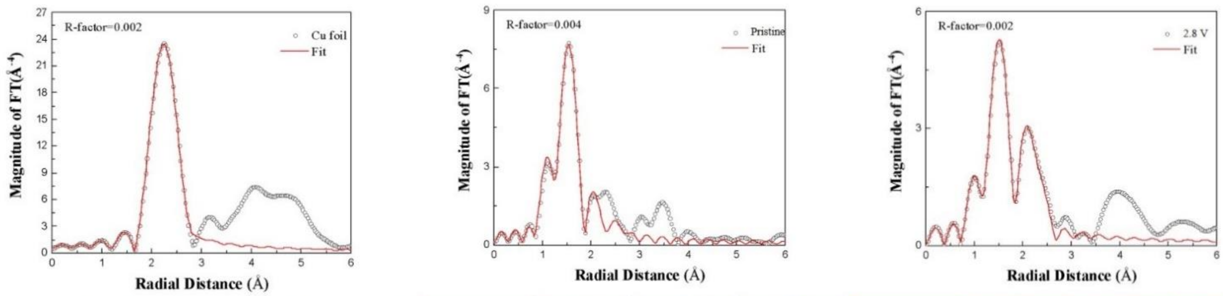

	N	R (Å)	σ² (Å²)
Cu-Cu	12	2.54	0.008

	N	R (Å)	σ² (Å²)
Cu-O/Cu-N	4	1.98	0.005
Cu-O	2	2.25	0.008

	N	R (Å)	σ² (Å²)
Cu-O/Cu-N	1.90	1.94	0.002
Cu-O	2.01	2.50	0.011

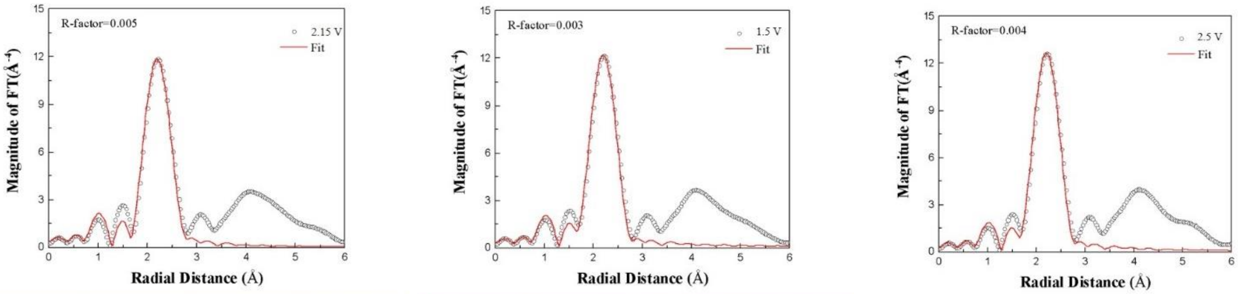

	N	R (Å)	σ² (Å²)
Cu-Cu	7.06	2.53	0.010

	N	R (Å)	σ² (Å²)
Cu-Cu	7.84	2.53	0.010

	N	R (Å)	σ² (Å²)
Cu-Cu	7.87	2.53	0.010

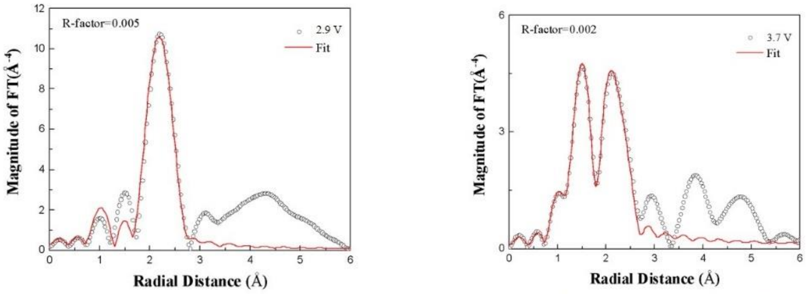

	N	R (Å)	σ² (Å²)
Cu-Cu	5.97	2.52	0.009

	N	R (Å)	σ² (Å²)
Cu-O/Cu-N	2.10	1.94	0.004
Cu-O	2.19	2.51	0.008

Fig. S16 *Ex situ* Cu K-edge EXAFS curve fitting of CP electrodes cycled at 20 mA g^{-1} (~0.08C) at different voltage positions (pristine; 2.80, 2.15 and 1.50 V during discharge; and 2.50, 2.90 and 3.70 V during charge). There are two types of Cu–O bonds in the crystal structure of $[CuL(Py)_2]_n$. In EXAFS fitting, the bond length of the shorter Cu–O is not distinguishable from that of Cu–N. The circle curves are the observed data and the solid lines are the best fit from the parameters in the corresponding tables (N = coordination number; R = bond length, Å; σ^2 = Debye–Waller factor, Å^2).

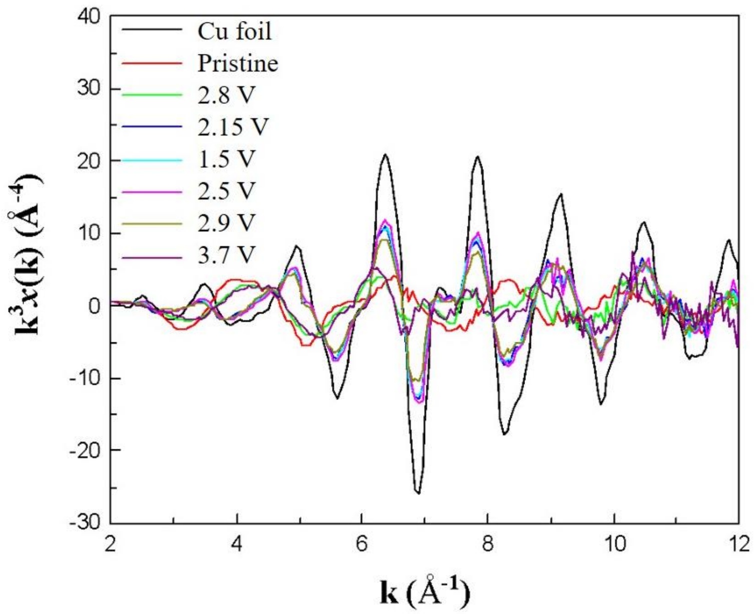

Fig. S17 Fourier-transformed $k^3\chi(k)$ vs. k EXAFS spectra for the CP electrodes cycled at 20 mA g^{-1} (~0.08C) together with references.

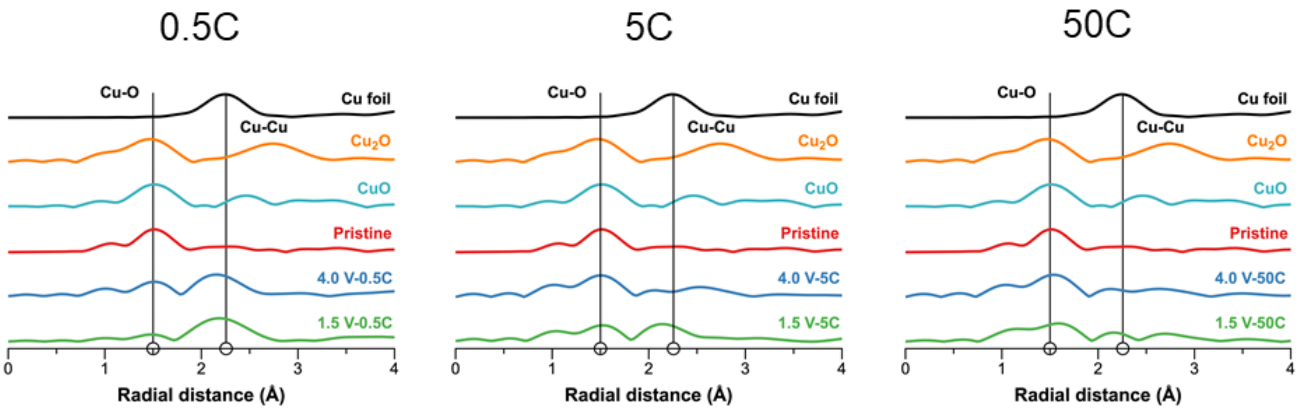

Fig. S18 *Ex situ* Cu K-edge EXAFS patterns of the CP electrodes cycled at 0.5C, 5C and 50C at end of discharge (1.5 V) and end of charge (4.0 V) together with the references.

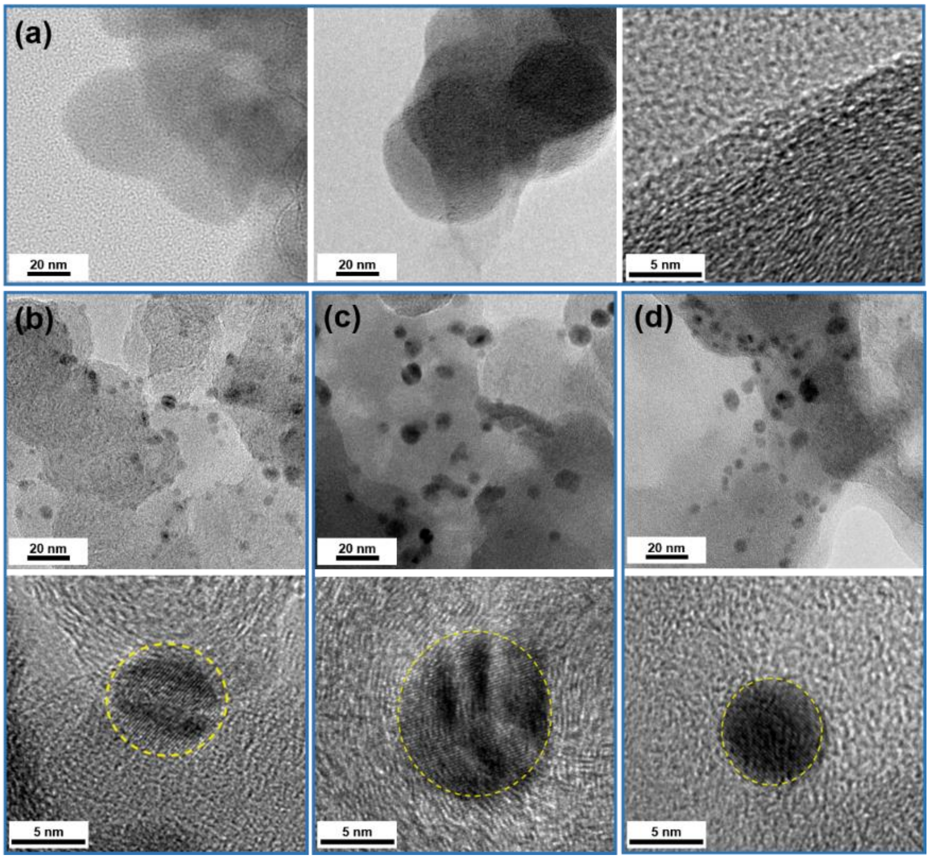

Fig. S19 HR-TEM images of CP electrodes cycled at 20 mA g^{-1} (~0.08C) (a) pristine, (b) at 2.8 V, (c) at 1.5 V and (d) at 4.0 V.

HR-TEM imaging was conducted on the CP electrodes to further investigate the change during discharge-charge cycles. TEM images in Fig. S19 show that when the CP is discharged to 2.8 and 1.5 V at a rate of 20 mA g^{-1} (~0.08C), metallic Cu nanoparticles are found to slightly aggregate with a size of ~5−10 nm. This is confirmed by the interplanar spacing of 0.21 nm which can be ascribed to the (111) plane of Cu metal.[10] On charge to 4.0 V, some Cu particles still can be observed. *Ex situ* electrodes from different rates were also investigated. At 0.5C and 3C (Fig. S20a and S20b), Cu nanoparticles can be found, similar to the case of 0.08C (20 mA g^{-1}, Fig. S19). As the rate gets higher, the amount of metallic Cu seems to be lower. Interestingly, at the rates of 5C and above (Fig. S20c and S20d), there are no longer Cu(0) particles found in the electrodes both at the end of discharge (1.5 V) and end of charge (4.0 V). These results suggest that the reduction to Cu(0) tends to take place at rates below 5C. When the cycling rate is above this threshold, the Cu centres may not be easily accessible or have enough time to react due to the kinetic effects. The lower degree of Cu aggregation in the CP electrodes at high rates also supports the better capacity retention observed in Fig. 2 (main text). This phenomenon that metal centres are reduced to a different degree of valence state at different cycling rates has never been reported in any metal-organic cathode materials. Instead, the majority of Cu-based CP or MOF electrodes only utilize one electron transfer between Cu(II) and Cu(I).[17-19]

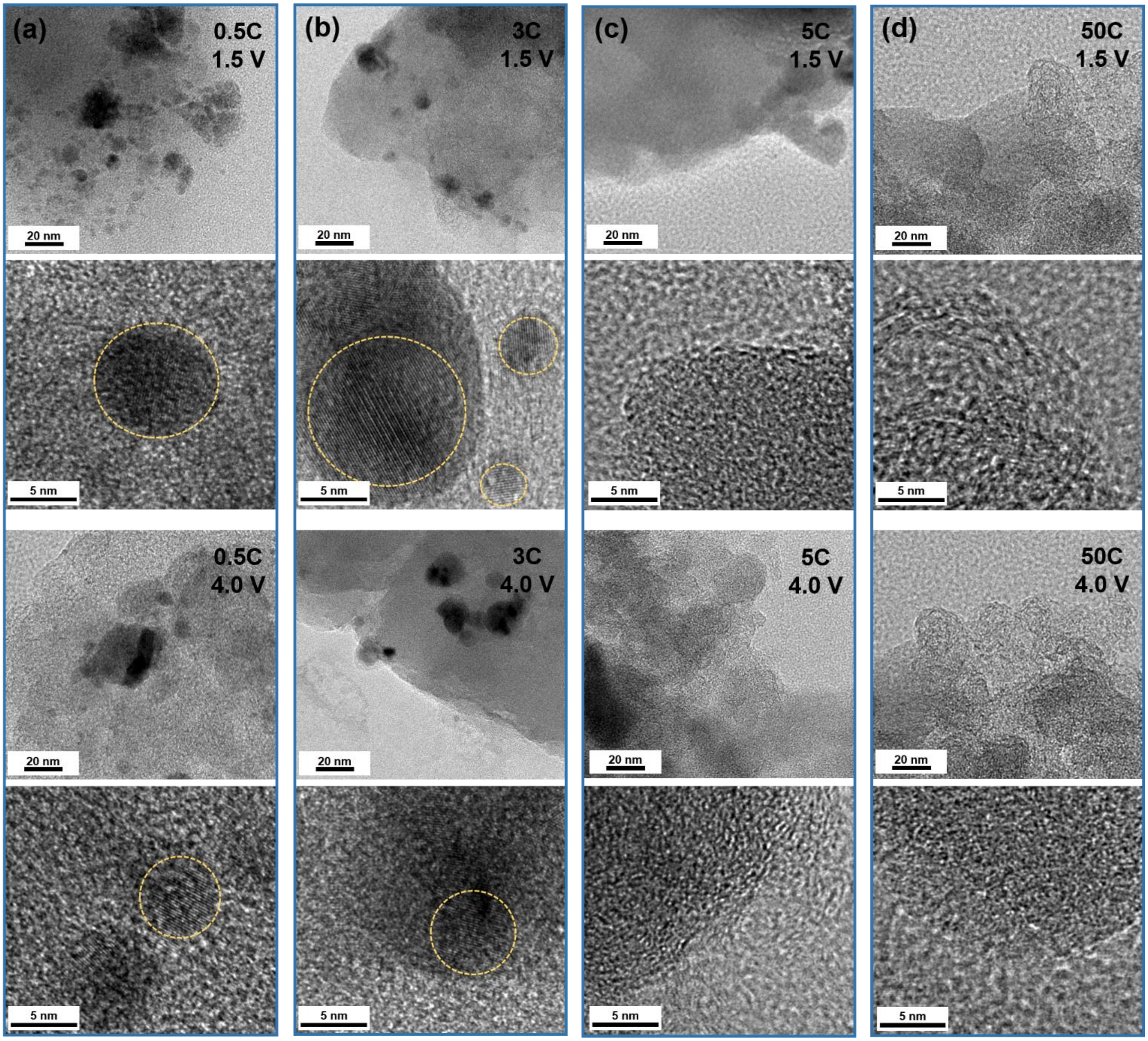

Fig. S20 HR-TEM images of CP electrodes at rates of 0.5C (a), 3C (b), 5C (c) and 50C (d) at 1.5 V on discharge and 4.0 V on charge.

Li⁺ Diffusion Coefficients by GITT

GITT was performed to determine Li⁺ diffusion coefficient (D_{Li^+}). From the potential response to a small constant current pulse (20 mA g⁻¹), D_{Li^+} can be calculated by the following equation:[20,21]

$$D_{Li^+} = \frac{4}{\pi\tau}\left(\frac{m_B V_M}{M_B A}\right)^2 \left(\frac{\Delta E_s}{\Delta E_\tau}\right)^2$$

where τ is the constant current pulse time (s); m_B is the mass of the active material in an electrode (g); M_B is molecular weight of the material (g mol⁻¹); V_M is the molar volume of the active material (cm³ mol⁻¹, calculated from the molecular weight and density); A is the electrode area (cm², diameter of 1.2 cm); ΔE_s is the change in cell voltage during open circuit period (V, 3 h rest time); ΔE_τ is the change in cell voltage during constant current pulse (V, 15 min duration).

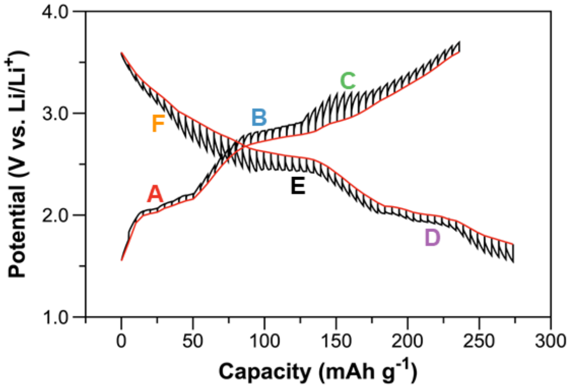

Position	D_{Li^+} (cm² s⁻¹)
A	1.79 x 10^{-10}
B	8.00 x 10^{-12}
C	2.83 x 10^{-12}
D	1.10 x 10^{-11}
E	8.10 x 10^{-13}
F	3.23 x 10^{-11}

Fig. S21 Left: GITT discharge-charge curves of $[CuL(Py)_2]_n$. Red curve is constructed from the last data point of each relaxation period. Right: the calculated Li diffusion coefficients.

GITT (Fig. S21) is used to determine quasi-equilibrium potentials at different stages during cell cycling. Overall, $[CuL(Py)_2]_n$ is found to have better kinetics with smaller overpotential compared to $[CuL(DMF)_2]_n$ previously reported.[10] This may be explained by the capping molecule pyridine axially-coordinated to the Cu which allows π-interactions, thus stabilizing the CP structure and promoting better charge transfer kinetics. It is worth noting that at potential close to the Cu redox couple, the overpotential appears to be larger than that of the organic redox centres, which indicates the faster redox kinetics of the organic ligand. These results reveal that the redox reaction presumably prefers to take place on the organic moieties especially at high cycling rates. This is consistent with the experimental results observed in XPS, XAS and HR-TEM at different cycling rates. The GITT data were also used to determine the Li-ion diffusion coefficients of the CP to be in the order of 10^{-10} to 10^{-13} cm² s⁻¹ (Fig. S21) which agree well with the values obtained from CV curves at different scan rates (Fig. S22).[22]

Li⁺ Diffusion Coefficients by Cyclic Voltammetry (CV)

The diffusion coefficient value D_{Li^+} can be calculated from the following equation:[22-25]

$$I_p = 2.69 \times 10^5 \, n^{3/2} A D_{Li^+}{}^{1/2} C v^{1/2}$$

where I_p is the peak current (A); n of the number of electrons per formula unit; A is the area of the electrode (cm^2, diameter of 1.2 cm); C is the concentration of Li$^+$ in electrolyte (10^{-3} mol cm^{-3}); v is the scan rate (V s^{-1}).

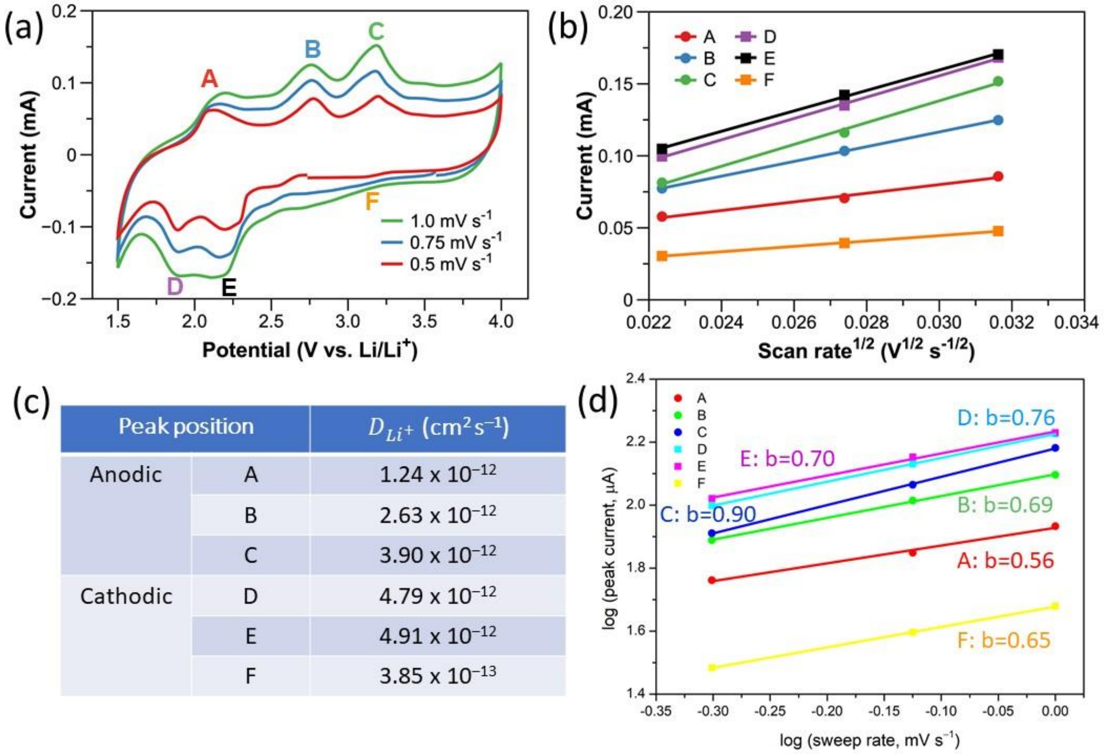

Peak position		D_{Li^+} (cm^2 s^{-1})
Anodic	A	1.24 x 10^{-12}
	B	2.63 x 10^{-12}
	C	3.90 x 10^{-12}
Cathodic	D	4.79 x 10^{-12}
	E	4.91 x 10^{-12}
	F	3.85 x 10^{-13}

Fig. S22 (a) CV curves of [CuL(Py)$_2$]$_n$ at different scan rates. (b) Relationship between the peak current and square root of scan rate together with (c) Li diffusion coefficients. (d) Relationship between log i (peak current) and log v (scan rate) from the CV curves in (a). The analysis of charge storage process was performed on [CuL(Py)$_2$]$_n$ with b values calculated from $i = av^b$.[17,26] The measured current i is fit to a power law with scan rate v, and b can be determined from the slope of the log i vs. log v. This analysis shows that the Faradaic charge storage associated with the peak maxima in CV of [CuL(Py)$_2$]$_n$ has a significant diffusion contribution; therefore, it is largely diffusion controlled charge storage mechanism within these scan rates tested (b = 0.5 indicating traditional diffusion dominated charge storage, while b = 1 indicating capacitor-like charge storage).

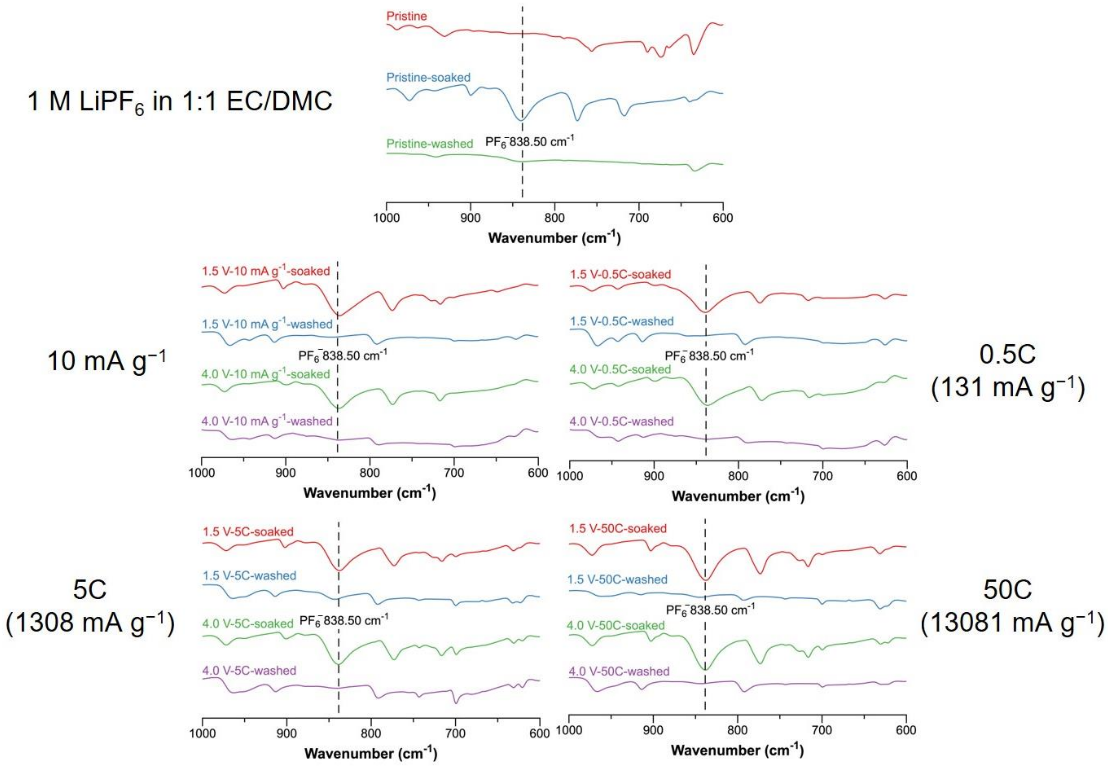

Fig. S23 The *ex situ* FT-IR spectra of $[CuL(Py)_2]_n$ electrodes (before and after washing) cycled at different rates to end of discharge (1.5 V) and end of charge (4.0 V), compared to the pristine electrode. At any cycling rate and voltage position, PF_6^- signal (~840 cm^{-1}) can only be observed in electrodes that were soaked in the $LiPF_6$ electrolyte. Once the electrodes were washed and the electrolyte was removed from the electrode surface, PF_6^- signal can no longer be observed. This provides evidence for the absence of PF_6^- anions in the CP structure during electrochemical cycling. This is also consistent with the result from single-crystal XRD of the CP showing close-packing of the 1D chains, which does not provide enough space for PF_6^- to transport.

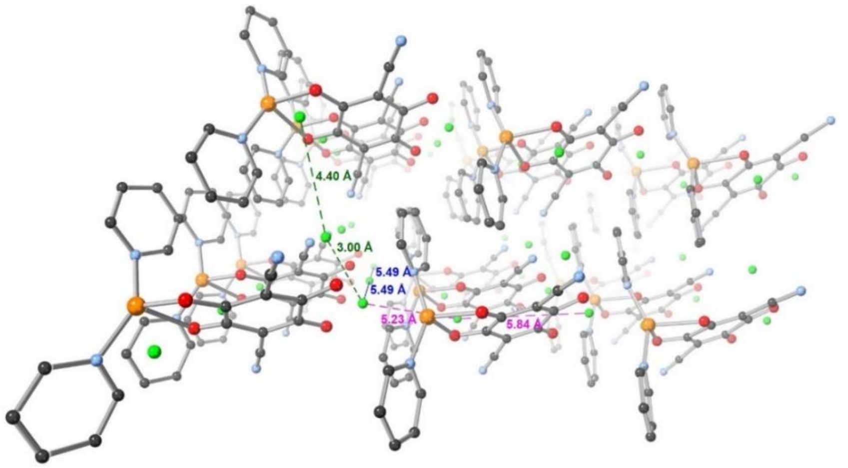

Fig. S24 The measured distances between inserted Li ions from simulated [CuL(Py)$_2$Li$_3$]$_n$ structure, which are within the ideal hopping distances of 2.99~5.84 Å for Li$^+$ ions. Colours of atoms: orange: Cu(I); gray: C; red: O; cyan: N; green: Li. Hydrogen atoms are omitted for clarity.

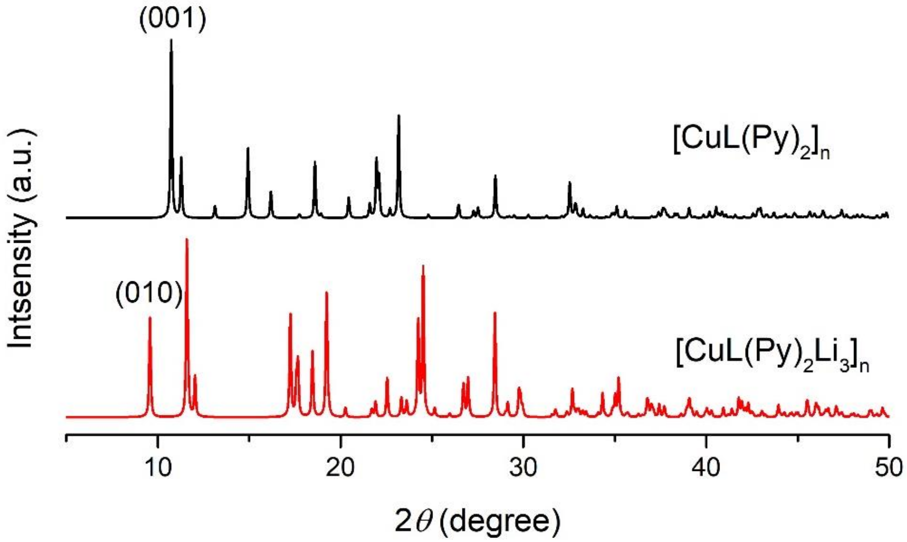

Fig. S25 Simulated PXRD patterns of [CuL(Py)$_2$]$_n$ and [CuL(Py)$_2$Li$_3$]$_n$.

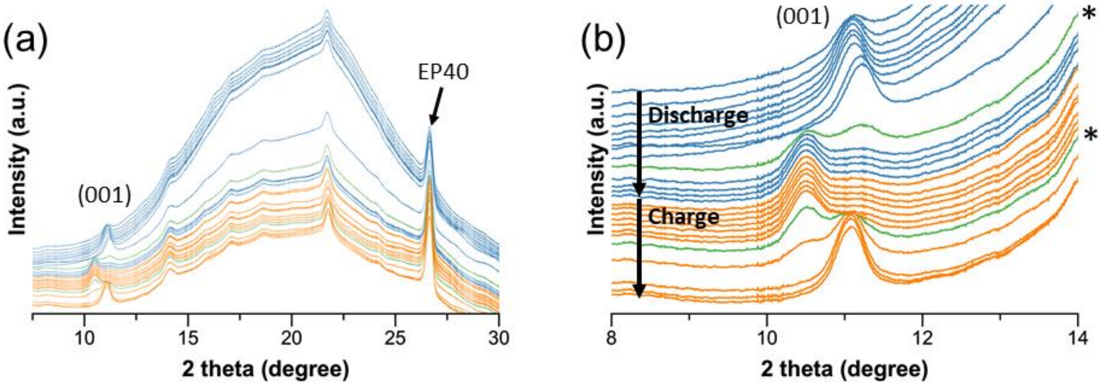

Fig. S26 *In situ* synchrotron PXRD of $[CuL(Py)_2]_n$ showing changes during cycling from open circuit voltage to 1.5 V (discharge), and up to 4.0 V (charge): (a) pattern from 7.5 to 30 degrees (with a peak from EP40 carbon substrate); and (b) pattern from 8 to 14 degrees showing a reversible shift of the $[CuL(Py)_2]_n$ peak during cycling.

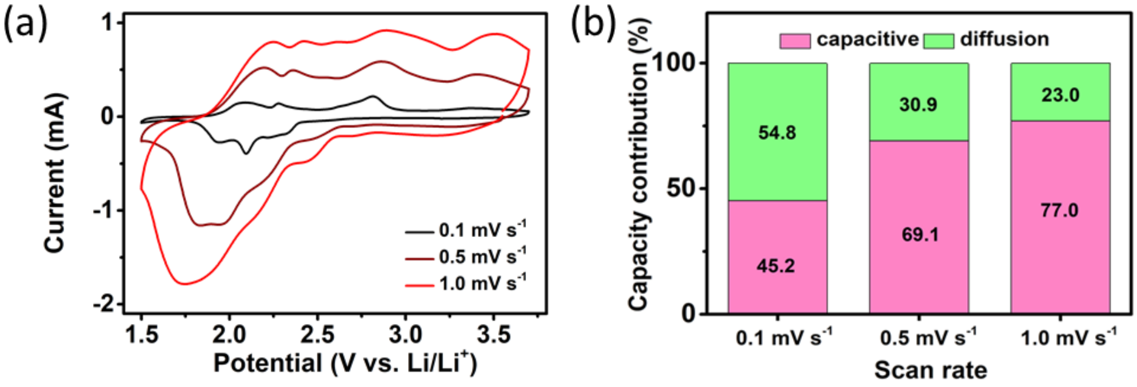

Fig. S27 (a) CV curves of $[CuL(Py)_2]_n$ at different scan rates. (b) Capacity contribution at different scan rates. To further quantitatively differentiate the contribution of the capacitive and diffusion-controlled elements to the overall capacity, the relationship $i = av^b$ can be divided into two terms: the capacitive effects ($k_1 v$) and diffusion-limited effects ($k_1 v^{1/2}$) as follows: $i = k_1 v + k_1 v^{1/2}$, where i is the current (A) at a fixed potential. By plotting $v^{1/2}$ vs $i/v^{1/2}$, k_1 and k_2 are derived from the slope and the y-axis intercept, respectively. As shown here, the ratio of stored charge contributed by capacitive process increases with the scan rate. This suggests that at a low rate, the bulk diffusion-controlled process is dominating, while at a high rate, a higher proportion of capacitive contribution is observed confirming an excellent rate performance of $[CuL(Py)_2]_n$ cathode.[27-29]

Energy Density and Power Density Calculation

From the electrochemical measurements of the CP, the maximum capacity delivered (C) and the average operating voltage ($V_{average}$) can be obtained. The energy density of the CP ($E_{electrode}$ in Wh kg^{-1}) may be simplified as:[30,31]

$$E_{electrode} = C \times V_{average}$$

The discharge time (t) may be used to calculate the power density of the CP ($P_{electrode}$ in W kg^{-1}) at a specific rate as shown in the following equation:[30,31]

$$P_{electrode} = \frac{E_{electrode}}{t}$$

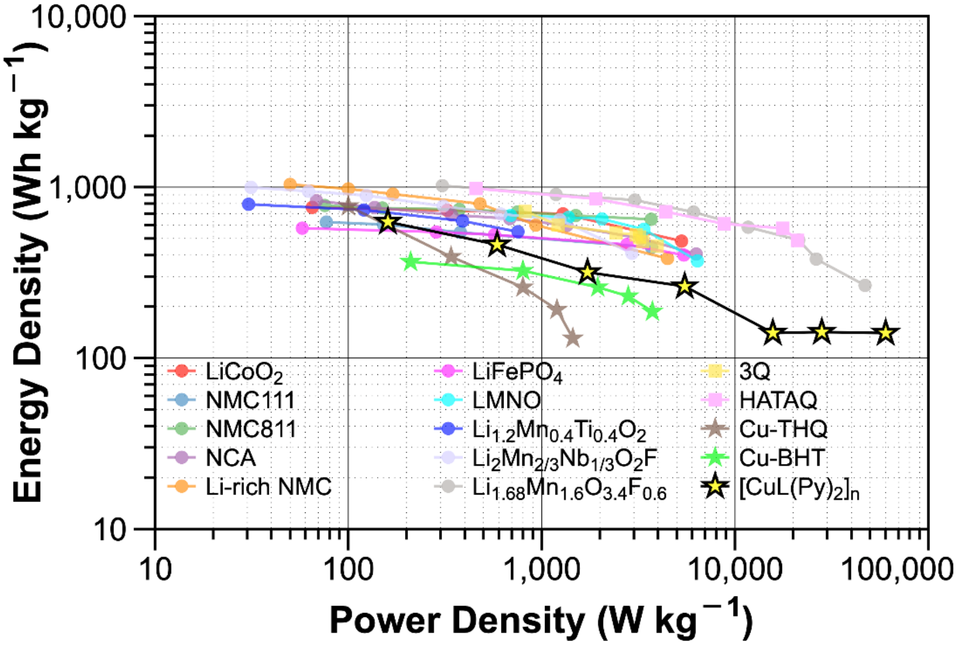

Fig. S28 Ragone plot comparing the energy and power density of [CuL(Py)$_2$]$_n$ to those of state-of-the-art Li-ion cathodes. Inorganic-based materials (circle) currently used in commercial LIBs and those recently reported[31] together with organic-based (square) and metal-organic-based (star) cathodes with the best performance in the literature (LiCoO$_2$,[32] NMC111,[33] NMC811,[33] NCA,[34] Li-rich NMC,[35] LiFePO$_4$,[36] LMNO,[37] Li$_{1.2}$Mn$_{0.4}$Ti$_{0.4}$O$_2$,[38] Li$_2$Mn$_{2/3}$Nb$_{1/3}$O$_2$F,[39] Li$_{1.68}$Mn$_{1.6}$O$_{3.4}$F$_{0.6}$,[31] 3Q,[30] HATAQ,[40] Cu-THQ[17] and Cu-BHT[41]). The electrochemical conditions for the cited materials are summarized in Table S1.

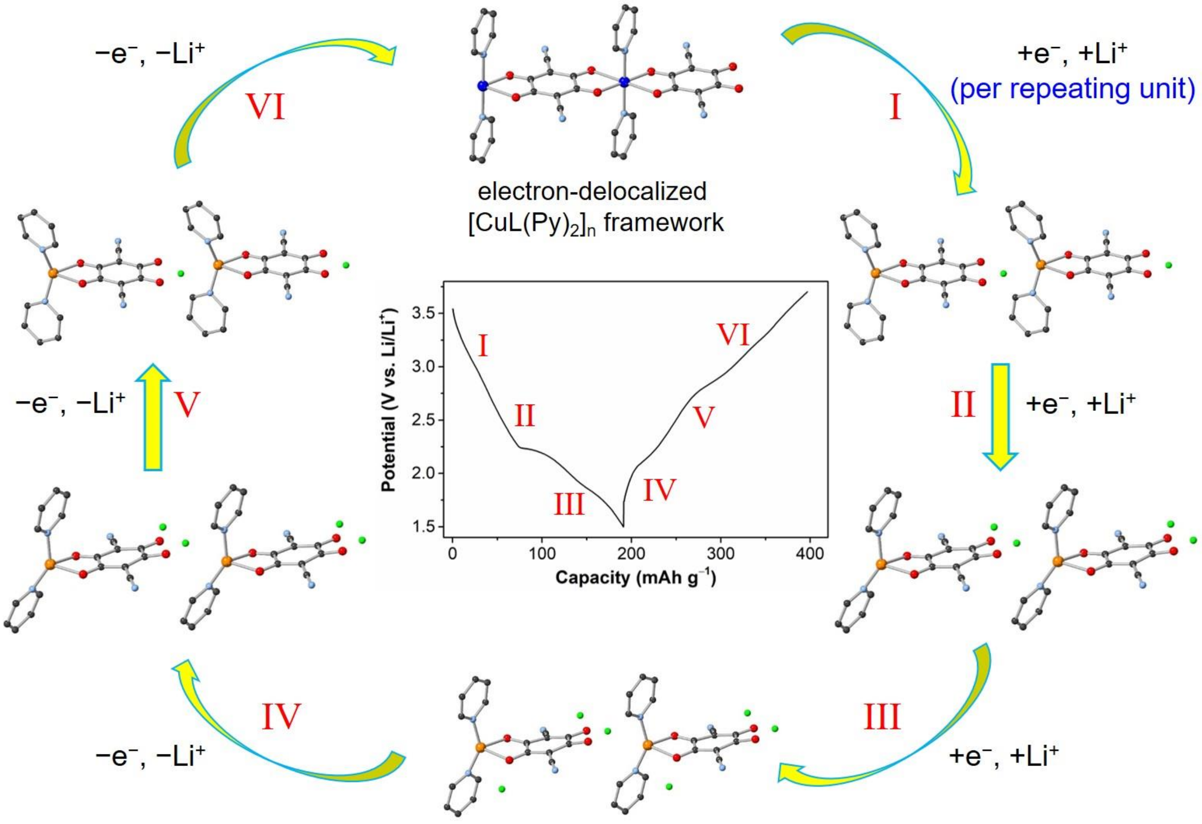

Fig. S29 Reversible evolution of the electronic states of $[CuL(Py)_2]_n$ in the case of three-electron transfer together with charge-discharge curve at 262 mA g^{-1}. The six stages marked by I–VI represent the different charge-discharge processes of the CP. Colours of atoms: blue: Cu(II); orange: Cu(I); grey: C; red: O; cyan: N; green: Li; the hydrogen atoms are omitted for clarity.

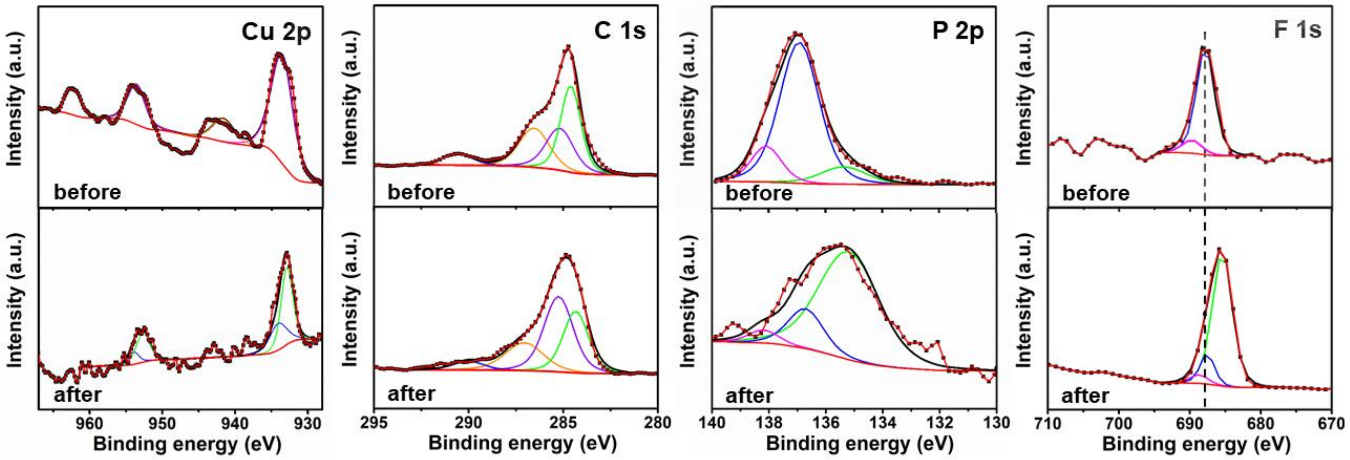

Fig. S30 Cu 2p, C 1s, P 2p and F 1s XPS spectra of the [CuL(Py)$_2$]$_n$ electrodes before and after discharge to 1.5 V in 1 M LiPF$_6$ in 1:1 v/v EC/DMC at 20 mA g^{-1} (~0.08C) (Cu 2p: pink: Cu(II); orange: satellite peak; blue: Cu(I); green: Cu(0); C 1s: green: C−C; purple: C−O; orange: C=O; blue: π−π* satellite peak; P 2p: pink: LiPF$_6$; blue: Li$_x$PF$_y$; green: Li$_x$PO$_y$F$_z$; F 1s: pink: PF$_x$; blue: Li$_x$PF$_y$; green: LiF).

XPS data in Fig. S30 reveal the surface change of the electrodes before and after cycling. Cu 2p and C 1s XPS spectra indicate the redox processes of the Cu metal centres and the organic moieties. Before discharge, the Cu ions in [CuL(Py)$_2$]$_n$ are Cu(II) as confirmed by Cu 2p$_{3/2}$ and Cu 2p$_{1/2}$ at 933.6 and 953.6 eV, respectively, in combination with the Cu 2p$_{3/2}$ satellite peak at ~942 eV,[11,42,43] while at the end of discharge, the spectrum shows the presence of Cu(I) and Cu(0) similar to the ex-situ XPS data in Fig. S10. The C 1s spectra reveal that the carbonyl group is transformed into an enol structure as witnessed in Fig. S11. It is worth noting that the signals which are mainly derived from the electrolyte solvents may also overlap with the C 1s signals from the CP.[44] In addition, the P 2p and F 1s data indicate the decomposition of the electrolyte LiPF$_6$. The P 2p spectrum before cycling shows that the major species are Li$_x$PF$_y$ (136.9 eV) and LiPF$_6$ (138.1 eV), whereas after cycling, Li$_x$PO$_y$F$_z$ appears to be the major phase observed at 135.4 eV.[45,46] For the F 1s before discharge, the dominant peak is observed due to the presence of LiPF$_6$ from the electrolyte (Li$_x$PF$_y$ at 687.9 and PF$_x$ at 689.8 eV). At the end of discharge, a large peak is present at 685.4 eV corresponding to the formation of LiF, which is known as a main decomposition product of LiPF$_6$.[45]

Table S1 Testing Parameters and Conditions of State-of-the-art Li-ion Cathodes Listed in Fig. S28.

Compound	Chemical Formula or Structure	Testing Conditions/Results	Reference
$LiCoO_2$	$LiCoO_2$	Micron-sized particles with $BaTiO_3$ coating; 3.3–4.5 V; 20 wt% carbon; rates 0.1C–10C (16–1600 mA g^{-1}) **data shown for 5 cycles at 1600 mA g^{-1}	32
NMC111	$LiNi_{1/3}Mn_{1/3}Co_{1/3}O_2$	~10 nm particles; 2.7–4.3 V; charge rate is constant at 40 mA g^{-1}; 7.5 wt% carbon; rates 0.2C–5C (40–1000 mA g^{-1}) **data shown for 1 cycle at 1000 mA g^{-1}	33
NMC811	$LiNi_{0.8}Mn_{0.1}Co_{0.1}O_2$	~10 nm particles; 2.7–4.3 V; charge rate is constant at 40 mA g^{-1}; 7.5 wt% carbon; rates 0.2C–5C (40–1000 mA g^{-1}) **data shown for 1 cycle at 1000 mA g^{-1}	33
NCA	$LiNi_{0.8}Co_{0.15}Al_{0.05}O_2$	Micron-sized particles; 2.7–4.3 V; 10 wt% carbon; rates 0.1C–10C (18–1800 mA g^{-1}) **data shown for 1 cycle at 10C	34
Li-rich NMC	$Li_{1.2}Mn_{0.525}Ni_{0.175}Co_{0.1}O_2$ or $0.6Li[Li_{1/3}Mn_{2/3}]O_2$– $0.4Li[Mn_{0.3}Ni_{0.45}Co_{0.25}]O_2$ solid solution	5–15 µm particles mixed with carbon nanofibre; 2.5–4.9 V; held voltage at 4.9 V until current < C/50; 7.5 wt% carbon; rates 0.05C–5C **data shown for 5 cycles at 5C	35
$LiFePO_4$	$LiFePO_4$	100–300 nm particles; 2.0–4.5 V; 10 wt% carbon; rates 0.1C–10C **data shown for 33 cycles at 10C	36
LNMO	$LiNi_{0.5}Mn_{1.5}O_4$	~0.5–1 µm particles; 3.5–5.0 V; charge rate is constant at 1C (1.18 mA cm^{-2}); 7.5 wt% carbon; rates 1C–10C (1.18–11.8 mA cm^{-2}) **data shown up to 5 cycles at 11.8 mA cm^{-2}	37
$Li_{1.2}Mn_{0.4}Ti_{0.4}O_2$	$Li_{1.2}Mn_{0.4}Ti_{0.4}O_2$	~100 nm particles; 1.5–4.7 V; 20 wt% carbon; rates 10–260 mA g^{-1} **data shown for 1 cycle at 260 mA g^{-1}	38
$Li_2Mn_{2/3}Nb_{1/3}O_2F$	$Li_2Mn_{2/3}Nb_{1/3}O_2F$	~100 nm particles; synthesized by ball-mill; 1.5–5.0 V; 20 wt% carbon; rates 10–1000 mA g^{-1} **data shown for 25 cycles at 1000 mA g^{-1}	39

Compound	Chemical Formula or Structure	Testing Conditions/Results	Reference
$Li_{1.68}Mn_{1.6}O_{3.4}F_{0.6}$	$Li_{1.68}Mn_{1.6}O_{3.4}F_{0.6}$	~100 nm particles; synthesized by ball-mill; 1.5–4.8 V; 20 wt% carbon for up to 2000 mA g^{-1} and 50 wt% carbon for higher rates; rates 100–20000 mA g^{-1} **data shown for 1 cycle at 20000 mA g^{-1}	31
3Q or triquinoxalinylene	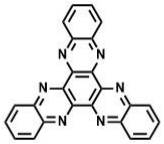	~200-nm-diameter rods; 1.2–3.9 V; 60 wt% graphene; rates 1C–20C (400–8000 mA g^{-1}) **data shown up to 10000 cycles at 8000 mA g^{-1}	30
HATAQ or hexaazatrianthranylene (HATA) embedded quinone	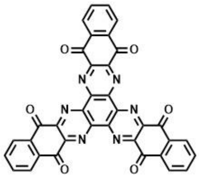	~0.5–1 μm particles; 1.2–3.9 V; 60 wt% carbon; rates 0.4C–19C (200–10000 mA g^{-1}) **data shown up to 1000 cycles at 10000 mA g^{-1}	40
Cu-THQ	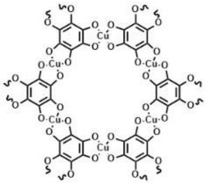 $Cu_3(C_6O_6)_2(NH_3CH_2CH_2NH_3)_{1.5}$	<50 nm particles; 1.2–4.0 V; 20 wt% graphene; rates 50–1000 mA g^{-1} **data shown up to 5 cycles at 1000 mA g^{-1}	17
Cu-BHT	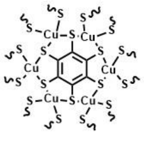 $[Cu_3(C_6S_6)]_n$	~1 μm particles; 1.5–3.0 V; 20 wt% MW-CNTs; rates 100–2000 mA g^{-1} **data shown for 3 cycles at 2000 mA g^{-1}	41
$[CuL(Py)_2]_n$	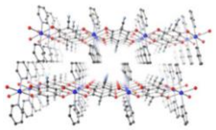 $[Cu(C_6O_4(CN)_2)(C_5H_5N)_2]_n$	Micron-sized particles; 1.5–3.7 V; 60 wt% carbon; rates 0.25C–100C (65–26162 mA g^{-1}) **data shown for 1000 cycles at 26162 mA g^{-1}	This work

Table S2 CP-based Cathode Materials for Li-ion Batteries Reported in the Literature.

1D CPs	Electrode Composition (active material (AM): conductive carbon: binder)	Electrolyte	Theoretical Capacity (Electron Transfer)	Voltage Window (V)	Initial Capacity at Lowest Rate	Reversible Capacity at Highest Rate	Capacity Retention at Highest Rate	Ref.
$[\mathrm{CuL(Py)_2}]_n$	**AM**:KB:PVDF (30:60:10)	1 M $\mathrm{LiPF_6}$ in 1:1 v/v EC/DMC	262 mAh $\mathrm{g^{-1}}$ (4 $\mathrm{e^-}$)	1.5–3.7	255 mAh $\mathrm{g^{-1}}$ at 0.25C (65 mA $\mathrm{g^{-1}}$)	59 mAh $\mathrm{g^{-1}}$ at 100C (26162 mA $\mathrm{g^{-1}}$)	81 % after 1000 cycles	This work
$[\mathrm{CuL(DMF)_2}]_n$	**AM**:Super P:graphite KS4:PVDF (30:50:10:10)	1 M $\mathrm{LiPF_6}$ in 1:1 v/v EC/DMC	268 mAh $\mathrm{g^{-1}}$ (4 $\mathrm{e^-}$)	1.5–3.7	268 mAh $\mathrm{g^{-1}}$ at 30 mA $\mathrm{g^{-1}}$	213 mAh $\mathrm{g^{-1}}$ at 120 mA $\mathrm{g^{-1}}$	43 % after 44 cycles	10
$[\mathrm{FePcOC(tz)}]_n$	**AM**:AB:PVDF (65:20:15)	1 M $\mathrm{LiPF_6}$ in 1:1 v/v PC/DMC	99.8 mAh $\mathrm{g^{-1}}$ (3 $\mathrm{e^-}$)	1.0–3.2	100 mAh $\mathrm{g^{-1}}$ at 70 μA $\mathrm{cm^{-2}}$	98 mAh $\mathrm{g^{-1}}$ at 70 μA $\mathrm{cm^{-2}}$	98 % after 50 cycles	47
$[\mathrm{FePcOC(dib)}]_n$	**AM**:AB:PVDF (60:25:15)	1 M $\mathrm{LiPF_6}$ in DME	147 mAh $\mathrm{g^{-1}}$ (5 $\mathrm{e^-}$)	1.8–4.3	147 mAh $\mathrm{g^{-1}}$ at 70 μA $\mathrm{cm^{-2}}$	147 mAh $\mathrm{g^{-1}}$ at 70 μA $\mathrm{cm^{-2}}$	100 % after 50 cycles	48
NiTIB	**AM**:AB:PTFE (60:35:5)	1 M $\mathrm{LiPF_6}$ in 1:1 v/v EC/DMC	n/a	1.5–4.1	155 mAh $\mathrm{g^{-1}}$ at 50 mA $\mathrm{g^{-1}}$	40 mAh $\mathrm{g^{-1}}$ at 500 mA $\mathrm{g^{-1}}$	20 % after 100 cycles	49
CuTIB	**AM**:AB:PTFE (60:35:5)	1 M $\mathrm{LiPF_6}$ in 1:1 v/v EC/DMC	n/a	1.5–4.1	262 mAh $\mathrm{g^{-1}}$ at 50 mA $\mathrm{g^{-1}}$	150 mAh $\mathrm{g^{-1}}$ at 1000 mA $\mathrm{g^{-1}}$	60 % after 100 cycles	49

2D CPs	Electrode Composition (active material (AM): conductive carbon: binder)	Electrolyte	Theoretical Capacity (Electron Transfer)	Voltage Window (V)	Initial Capacity at Lowest Rate	Reversible Capacity at Highest Rate	Capacity Retention at Highest Rate	Ref.
$[Li_2(C_6H_2O_4)]$	**AM**:AB:PTFE (60:35:5)	1 M $LiPF_6$ in 1:1 v/v EC/DMC	n/a	1.5–3.5	176 mAh g^{-1} at 100 mA g^{-1}	138 mAh g^{-1} at 100 mA g^{-1}	78 % after 10 cycles	50
$\{[Cd(ClO_4)_2(DPNDI)_2]\cdot(DMA)_{4.5}\cdot(H_2O)_2\}_n$	**AM**:Super P:PVDF (45:45:10)	1 M $LiPF_6$ in 1:1:1 v/v EC/DEC/DMC	n/a	1.8–3.4	46.8 mAh g^{-1} at 100 mA g^{-1}	37 mAh g^{-1} at 100 mA g^{-1}	78 % after 50 cycles	51
$\{[Co(NCS)_2(DPNDI)_2]\cdot(DMA)\cdot(H_2O)_5\}_n$	**AM**:Super P:PVDF (45:45:10)	1 M $LiPF_6$ in 1:1:1 v/v EC/DEC/DMC	n/a	1.8–3.4	62.7 mAh g^{-1} at 100 mA g^{-1}	6 mAh g^{-1} at 100 mA g^{-1}	9.6 % after 10 cycles	51
$Cu_3(HHTP)_2$	**AM**:PVDF (80:20)	1 M $LiPF_6$ in 1:1 v/v EC/DMC	96 mAh g^{-1} (3 e^-)	1.5–3.7	105 mAh g^{-1} at 1C	85 mAh g^{-1} at 20C	85 % after 500 cycles	52
Cu-THQ	**AM**:Graphene:sodium alga acid (70:20:10)	1 M $LiPF_6$ in 1:1 v/v EC/DEC	458 mAh g^{-1} (3 e^-)	1.2–4.0	387 mAh g^{-1} at 50 mA g^{-1} (2nd)	93 mAh g^{-1} at 1000 mA g^{-1}	~100% after 5 cycles	17
$Cu_3(HIB)_2$	**AM**:MWCNTs:PVDF (70:20:10)	1 M $LiPF_6$ in 3:7 v/v EC/DEC	n/a	2.5–4.25	~140 mAh g^{-1} at 5 mA g^{-1*}	~15 mAh g^{-1} at 250 mA g^{-1*}	~100% after 5 cycles	22
$Cu_3(TIPG)_2$	**AM**:MWCNTs:PVDF (70:20:10)	1 M $LiPF_6$ in 3:7 v/v EC/DEC	n/a	2.5–4.25	~60 mAh g^{-1} at 5 mA g^{-1*}	~7 mAh g^{-1} at 250 mA g^{-1*}	~100% after 5 cycles	22

Cu$_3$(HAB)$_2$	**AM**:MWCNTs:PVDF (70:20:10)	1 M LiPF$_6$ in 3:7 v/v EC/DEC	n/a	2.5–4.25	~300 mAh g^{-1} at 5 mA g^{-1}*	~100 mAh g^{-1} at 5 mA g^{-1}*	~33% after 7 cycles	22
Cu-BHT	**AM**: MWCNTs:PVDF (70:20:10)	1 M LiTFSI in 1:1 v/v DME/DOL	232 mAh g^{-1} (4 e$^-$)	1.5–3.0	174 mAh g^{-1} at 100 mA g^{-1}	100 mAh g^{-1} at 2000 mA g^{-1}*	~100% after 3 cycles	41
Cu-CuPc	**AM**:KB:PTFE (33:33:33)	1 M LiPF$_6$ in 1:1 v/v EC/DMC	304.3 mAh g^{-1} (10 e$^-$)	2.0–4.4	128 mAh g^{-1} at 13 mA g^{-1}	55 mAh g^{-1} at 130 mA g^{-1}	~65% after 200 cycles	53
NiDI	**AM**:MWCNTs:PVDF (70:20:10)	1 M LiPF$_6$ in 3:7 v/v EC/DEC	n/a	3.0–4.5	155 mAh g^{-1} at 10 mA g^{-1}	55 mAh g^{-1} at 500 mA g^{-1}	n/a	19
HHB-Cu NS	**AM**:Super P: alginate sodium (60:30:10)	1 M LiPF$_6$ in 1:1 v/v EC/DMC	n/a	1.3–2.6	153 mAh g^{-1} at 100 mA g^{-1}	~95 mAh g^{-1} at 2000 mA g^{-1}*	~100% after 5 cycles	54

3D CPs	**Electrode Composition (active material (AM): conductive carbon: binder)**	**Electrolyte**	**Theoretical Capacity (Electron Transfer)**	**Voltage Window (V)**	**Initial Capacity at Lowest Rate**	**Reversible Capacity at Highest Rate**	**Capacity Retention at Highest Rate**	**Ref.**
3D-DS-Mn-MOF	**AM**:Super P:PVDF (30:60:10)	1M LiClO$_4$ in TEGDME	186 mAh g^{-1}	1.6–4.2	160 mAh g^{-1} at 200 mA g^{-1} (5th)	~115 mAh g^{-1} at 200 mA g^{-1}*	~72% after 100 cycles	55
MIL-101(Fe)	**AM**:KB:PTFE (33:33:33)	1 M LiPF$_6$ in 1:2 v/v EC/DMC	n/a	2.0–4.2	107 mAh g^{-1} at 0.02C	60 mAh g^{-1} at 0.2C	120% after 100 cycles	56

MIL-53(Fe)·H_2O	**AM**:Super P (85:15)	1 M $LiPF_6$ in 1:1 v/v EC/DMC	n/a	1.5–3.5	80 mAh g^{-1} at C/40	72 mAh g^{-1} at C/40*	90% after 50 cycles	57
Cu(2,7-AQDC)	**AM**:CB:PVDF (10:70:20)	1 M $LiPF_6$ in 1:1 v/v EC/DEC	162 mAh g^{-1} (3 e^-)	1.7–4.0	147 mAh g^{-1} at 1 mA g^{-1}	105 mAh g^{-1} at 1 mA g^{-1}	71% after 50 cycles	18
Mn_7(2,7-AQDC)$_6$(2,6-AQDC) $(DMA)_6$	**AM**:CB:PVDF (10:70:20)	1 M $LiPF_6$ in 1:1 v/v EC/DEC	190 mAh g^{-1} (3 e^-)	1.3–4.5	205 mAh g^{-1} at 1 mA g^{-1} (2nd)	50 mAh g^{-1} at 20 mA g^{-1}	70% after 5 cycles	58
Cu-TCA	**AM**:Super P:PVDF (80:10:10)	1 M $LiPF_6$ in 1:1 v/v EC/DMC	145 mAh g^{-1}	1.4–4.3	102 mAh g^{-1} at 0.5C	45.1 mAh g^{-1} at 2C	71% after 200 cycles	59
SNNU-73	**AM**:AB:PVDF (60:30:10)	1 M $LiPF_6$ in 1:1:1 v/v/v EC/DEC/EMC	n/a	0.3–3.0	155.6 mAh g^{-1} at 50 mA g^{-1}	67.5 mAh g^{-1} at 50 mA g^{-1}	43% after 50 cycles	60
SNNU-76	**AM**:AB:PVDF (60:30:10)	1 M $LiPF_6$ in 1:1:1 v/v/v EC/DEC/EMC	n/a	0.3–3.0	87.9 mAh g^{-1} at 50 mA g^{-1}	41.5 mAh g^{-1} at 50 mA g^{-1}	47% after 50 cycles	60
V^{IV}(O)(bdc)	**AM**:AB:PVDF (65:30:5)	1 M $LiPF_6$ in 1:1 v/v EC/ EMC	n/a	1.6–4.0	118 mAh g^{-1} at 10 mA g^{-1}	37 mAh g^{-1} at 1200 mA g^{-1}*	n/a	61
CuFe-PBA@NiFe-PBA	**AM**:AB:PTFE (70:15:15)	1 M $LiClO_4$ in 1:1 v/v EC/ DEC	n/a	2.5–4.3	99 mAh g^{-1} at 10 mA g^{-1}	64 mAh g^{-1} at 10 mA g^{-1}*	65% after 50 cycles	62
$K_2Mn[Mn(CN)_6]$	**AM**:AB:PTFE (75:20:5)	1 M $LiClO_4$ in 1:1 v/v EC/ DEC	176 mAh g^{-1} (1.72 e^-)	2.5–4.3	197 mAh g^{-1} at 30 mA g^{-1}	130 mAh g^{-1} at 30 mA g^{-1}*	66% after 10 cycles	63

FeHCCo	**AM**:Super P:PVDF (70:20:10)	1 M $\mathrm{LiPF_6}$ in 1:1 v/v EC/ DEC	n/a	2.2–4.5	165 mAh g^{-1} at 0.3C (50 mA g^{-1})*	57 mAh g^{-1} at 6.25C*	~100% after 5 cycles*	64

Note: * indicates capacity taken from the rate capability plot or the discharge/charge profile. AB = acetylene black, CB = carbon black, KB = Ketjen black. EC = ethylene carbonate, PC = propylene carbonate, DEC = diethylene carbonate, DMC = dimethyl carbonate, DME = dimethyl ether, DOL = dioxolane, EMC = ethyl methyl carbonate, TEGDME = tetraethylene glycol dimethyl ether, MWCNTs = multiwall carbon nanotubes.

Table S3 Crystallographic Data of $[CuL(Py)_2]_n$.

Identification code	CPY
Empirical formula	$C_{18}H_{10}CuN_4O_4$
Formula weight	409.84
Temperature/K	200(2)
Crystal system	Triclinic
Space group	P−1
a/Å	6.2604(8)
b/Å	8.0667(9)
c/Å	8.9610(11)
α/°	72.023(3)
β/°	75.573(4)
γ/°	85.059(3)
Volume/Å^3	416.85(9)
Z	1
ρ_{calc} g/cm^3	1.633
μ/mm^{-1}	1.344
F(000)	207
Radiation	Mo Kα (λ = 0.71073)
2θ range for data collection/°	2.46 to 25.03
Index ranges	$-7 \le h \le 7, -9 \le k \le 9, -10 \le l \le 10$
Reflections collected	9033
Independent reflections	1468 [R_{int} = 0.0629, R_{sigma} = 0.0441]
Data/restraints/parameters	1468/0/124
Goodness-of-fit on F^2	1.067
Final R indexes [$I > 2\sigma (I)$]	R_1 = 0.0334, wR_2 = 0.0598
Final R indexes [all data]	R_1 = 0.0464, wR_2 = 0.0660
Largest diff. peak/hole / e Å^{-3}	0.267/-0.296

Table S4 Lattice Parameters of the $[CuL(Py)_2]_n$ Crystal Structure Obtained by X-ray Diffraction and DFT Calculations.

Method	*a* (Å)	*b* (Å)	*c* (Å)
Experiment (X-ray diffraction)	6.260	8.066	8.961
PBE-DFT-D3	6.124	8.213	8.883

Table S5 Comparison of Important Distances Obtained by X-ray Diffraction and DFT Calculations.

Method	Cu–O1	Cu–O2	Cu–N
Experiment (X-ray diffraction)	2.326	1.991	2.027
PBE-DFT-D3	2.389	2.044	2.017

References

1 G. Kresse and J. Hafner, *Phys. Rev. B*, 1993, **47**, 558–561.

2 G. Kresse and J. Hafner, *Phys. Rev. B*, 1994, **49**, 14251–14269.

3 G. Kresse and J. Furthmüller, *Phys. Rev. B*, 1996, **54**, 11169–11186.

4 G. Kresse and J. Furthmüller, *Comput. Mater. Sci.*, 1996, **6**, 15–50.

5 P. E. Blöchl, *Phys. Rev. B*, 1994, **50**, 17953–17979.

6 G. Kresse and D. Joubert, *Phys. Rev. B*, 1999, **59**, 1758–1775.

7 J. P. Perdew, K. Burke and M. Ernzerhof, *Phys. Rev. Lett.*, 1996, **77**, 3865–3868.

8 S. Grimme, J. Antony, S. Ehrlich and H. Krieg, *J. Chem. Phys.*, 2010, **132**, 154104.

9 P. Pulay, *Chem. Phys. Lett.*, 1980, **73**, 393–398.

10 C.-H. Chang, A.-C. Li, I. Popovs, W. Kaveevivitchai, J.-L. Chen, K.-C. Chou, T.-S. Kuo and T.-H. Chen, *J. Mater. Chem. A*, 2019, **7**, 23770–23774.

11 Z. Jin, C. Liu, K. Qi and X. Cui, *Sci. Rep.*, 2017, **7**, 39695.

12 J. Wang, Q. Deng, M. Li, K. Jiang, J. Zhang, Z. Hu and J. Chu, *Sci. Rep.*, 2017, **7**, 8903.

13 H. H. Lee, J. B. Lee, Y. Park, K. H. Park, M. S. Okyay, D.-S. Shin, S. Kim, J. Park, N. Park, B.-K. An, Y. S. Jung, H.-W. Lee, K. T. Lee and S. Y. Hong, *ACS Appl. Mater. Interfaces*, 2018, **10**, 22110–22118.

14 O. Müller, J. Stötzel, D. Lützenkirchen-Hecht and R. Frahm, *J. Phys.: Conf. Ser.*, 2013, **425**, 092010.

15 O. Müller, D. Lützenkirchen-Hecht and R. Frahm, *Rev. Sci. Instrum.*, 2015, **86**, 093905.

16 B. Ravel and M. Newville, *J. Synchrotron. Rad.*, 2005, **12**, 537–541.

17 Q. Jiang, P. Xiong, J. Liu, Z. Xie, Q. Wang, X.-Q. Yang, E. Hu, Y. Cao, J. Sun, Y. Xu and L. Chen, *Angew. Chem. Int. Ed.*, 2020, **59**, 5273–5277.

18 Z. Zhang, H. Yoshikawa and K. Awaga, *J. Am. Chem. Soc.*, 2014, **136**, 16112–16115.

19 K. Wada, K. Sakaushi, S. Sasaki and H. Nishihara, *Angew. Chem. Int. Ed.*, 2018, **57**, 8886–8890.

20 W. Ren, M. Qin, Z. Zhu, M. Yan, Q. Li, L. Zhang, D. Liu and L. Mai, *Nano Lett.*, 2017, **17**, 4713–

4718.

21 Y.-S. Lee and K.-S. Ryu, *Sci. Rep.*, 2017, **7**, 16617.

22 M. Amores, K. Wada, K. Sakaushi and H. Nishihara, *J. Phys. Chem. C*, 2020, **124**, 9215–9224.

23 S. Li, J. Lin, Y. Ding, P. Xu, X. Guo, W. Xiong, D.-Y. Wu, Q. Dong, J. Chen and L. Zhang, *ACS Nano*, 2021, **15**, 13803–13813.

24 Y. Wang, D. Zhang, C. Chang, L. Deng and K. Huang, *Mater. Chem. Phys.*, 2014, **148**, 933–939.

25 N. Ding, J. Xu, Y. X. Yao, G. Wegner, X. Fang, C. H. Chen and I. Lieberwirth, *Solid State Ionics*, 2009, **180**, 222–225.

26 J. B. Cook, H.-S. Kim, T. C. Lin, C.-H. Lai, B. Dunn and S. H. Tolbert, *Adv. Energy Mater.*, 2017, **7**, 1601283.

27 W. Wang, V. S. Kale, Z. Cao, S. Kandambeth, W. Zhang, J. Ming, P. T. Parvatkar, E. Abou-Hamad, O. Shekhah, L. Cavallo, M. Eddaoudi and H. N. Alshareef, *ACS Energy Lett.*, 2020, **5**, 2256–2264.

28 Z. Lin, H.-Y. Shi, L. Lin, X. Yang, W. Wu and X. Sun, *Nat. Commun.*, 2021, **12**, 4424.

29 J. Wang, J. Polleux, J. Lim and B. Dunn, *J. Phys. Chem. C*, 2007, **111**, 14925–14931.

30 C. Peng, G.-H. Ning, J. Su, G. Zhong, W. Tang, B. Tian, C. Su, D. Yu, L. Zu, J. Yang, M.-F. Ng, Y.-S. Hu, Y. Yang, M. Armand and K. P. Loh, *Nat. Energy*, 2017, **2**, 17074.

31 H. Ji, J. Wu, Z. Cai, J. Liu, D.-H. Kwon, H. Kim, A. Urban, J. K. Papp, E. Foley, Y. Tian, M. Balasubramanian, H. Kim, R. J. Clément, B. D. McCloskey, W. Yang and G. Ceder, *Nat. Energy*, 2020, **5**, 213–221.

32 T. Teranishi, Y. Yoshikawa, R. Sakuma, H. Okamura, H. Hashimoto, H. Hayashi, T. Fujii, A. Kishimoto and Y. Takeda, *ECS Electrochem. Lett.*, 2015, **4**, A137–A140.

33 H.-J. Noh, S. Youn, C. S. Yoon and Y.-K. Sun, *J. Power Sources*, 2013, **233**, 121–130.

34 N. Wu, H. Wu, W. Yuan, S. Liu, J. Liao and Y. Zhang, *J. Mater. Chem. A*, 2015, **3**, 13648–13652.

35 S. K. Martha, J. Nanda, G. M. Veith and N. J. Dudney, *J. Power Sources*, 2012, **199**, 220–226.

36 D. Choi and P. N. Kumta, *J. Power Sources*, 2007, **163**, 1064–1069.

37 J.-H. Cho, J.-H. Park, M.-H. Lee, H.-K. Song and S.-Y. Lee, *Energy Environ. Sci.*, 2012, **5**, 7124–7131.

38 H. Ji, A. Urban, D. A. Kitchaev, D.-H. Kwon, N. Artrith, C. Ophus, W. Huang, Z. Cai, T. Shi, J. C. Kim, H. Kim and G. Ceder, *Nat. Commun.*, 2019, **10**, 592.

39 J. Lee, D. A. Kitchaev, D.-H. Kwon, C.-W. Lee, J. K. Papp, Y.-S. Liu, Z. Lun, R. J. Clément, T. Shi, B. D. McCloskey, J. Guo, M. Balasubramanian and G. Ceder, *Nature*, 2018, **556**, 185–190.

40 M.-S. Wu, N. T. H. Luu, T.-H. Chen, H. Lyu, T.-W. Huang, S. Dai, X.-G. Sun, A. S. Ivanov, J.-C. Lee, I. Popovs and W. Kaveevivitchai, *Adv. Energy Mater.*, 2021, **11**, 2100330.

41 Z. Wu, D. Adekoya, X. Huang, M. J. Kiefel, J. Xie, W. Xu, Q. Zhang, D. Zhu and S. Zhang, *ACS Nano*, 2020, **14**, 12016–12026.

42 L. Kundakovic and M. Flytzani-Stephanopoulos, *Appl. Cat. A*, 1998, **171**, 13–29.

43 M. Konsolakis, S. A. C. Carabineiro, E. Papista, G. E. Marnellos, P. B. Tavares, J. A. Moreira, Y. Romaguera-Barcelay and J. L. Figueiredo, *Catal. Sci. Technol.*, 2015, **5**, 3714–3727.

44 X. Cao, X. Ren, L. Zou, M. H. Engelhard, W. Huang, H. Wang, B. E. Matthews, H. Lee, C. Niu, B. W. Arey, Y. Cui, C. Wang, J. Xiao, J. Liu, W. Xu and J.-G. Zhang, *Nat. Energy*, 2019, **4**, 796–805.

45 D. E. Arreaga-Salas, A. K. Sra, K. Roodenko, Y. J. Chabal and C. L. Hinkle, *J. Phys. Chem. C*, 2012, **116**, 9072–9077.

46 B. S. Parimalam, A. D. MacIntosh, R. Kadam and B. L. Lucht, *J. Phys. Chem. C*, 2017, **121**, 22733–22738.

47 S.-J. Kim, K. Onishi, M. Matsumoto and K. Shigehara, *J. Porphyrins Phthalocyanines*, 2001, **5**, 397–404.

48 Y. Asai, K. Onishi, S. Miyata, S.-J. Kim, M. Matsumoto and K. Shigehara, *J. Electrochem. Soc.*, 2001, **148**, A305.

49 R. R. Kapaev, S. Olthof, I. S. Zhidkov, E. Z. Kurmaev, K. J. Stevenson, K. Meerholz and P. A. Troshin, *Chem. Mater.*, 2019, **31**, 5197–5205.

50 J. Xiang, C. Chang, M. Li, S. Wu, L. Yuan and J. Sun, *Cryst. Growth Des.*, 2008, **8**, 280–282.

51 B. Tian, G.-H. Ning, Q. Gao, L.-M. Tan, W. Tang, Z. Chen, C. Su and K. P. Loh, *ACS Appl. Energy Mater.*, 2016, **8**, 31067–31075.

52 S. Gu, Z. Bai, S. Majumder, B. Huang and G. Chen, *J. Power Sources*, 2019, **429**, 22–29.

53 H. Nagatomi, N. Yanai, T. Yamada, K. Shiraishi and N. Kimizuka, *Chem. Eur. J.*, 2018, **24**, 1806–1810.

54 Z. Wang, G. Wang, H. Qi, M. Wang, M. Wang, S. Park, H. Wang, M. Yu, U. Kaiser, A. Fery, S. Zhou, R. Dong and X. Feng, *Chem. Sci.*, 2020, **11**, 7665–7671.

55 T. Shimizu, H. Wang, D. Matsumura, K. Mitsuhara, T. Ohta and H. Yoshikawa, *ChemSusChem*, 2020, **13**, 2256–2263.

56 T. Yamada, K. Shiraishi, H. Kitagawa and N. Kimizuka, *Chem. Commun.*, 2017, **53**, 8215–8218.

57 G. Férey, F. Millange, M. Morcrette, C. Serre, M.-L. Doublet, J.-M. Grenèche and J.-M. Tarascon, *Angew. Chem. Int. Ed.*, 2007, **46**, 3259–3263.

58 Z. Zhang, H. Yoshikawa and K. Awaga, *Chem. Mater.*, 2016, **28**, 1298–1303.

59 Z. Peng, X. Yi, Z. Liu, J. Shang and D. Wang, *ACS Appl. Mater. Interfaces*, 2016, **8**, 14578–14585.

60 Z.-Q. Du, Y.-P. Li, X.-X. Wang, J. Wang and Q.-G. Zhai, *Dalton Trans.*, 2019, **48**, 2013–2018.

61 W. Kaveevivitchai and A. J. Jacobson, *J. Power Sources*, 2015, **278**, 265–273.

62 D. Asakura, C. H. Li, Y. Mizuno, M. Okubo, H. Zhou and D. R. Talham, *J. Am. Chem. Soc.*, 2013, **135**, 2793–2799.

63 D. Asakura, M. Okubo, Y. Mizuno, T. Kudo, H. Zhou, K. Ikedo, T. Mizokawa, A. Okazawa and N. Kojima, *J. Phys. Chem. C*, 2012, **116**, 8364–8369.

64 K. Zhang, R. S. Varma, H. W. Jang, J.-W. Choi and M. Shokouhimehr, *J. Alloys Compd.*, 2019, **791**, 911–917.